A Study of Flow over a Rippled Bed using Particle Image Velocimetry

Heather Catherine Earnshaw

Doctor of Philosophy

The University of Edinburgh

1996

Abstract

Experiments have been performed in wave flumes to investigate the kinematics of flows over a rippled sea bed. Results from Particle Image Velocimetry (PIV) measurements of a variety of flows over sharp crested vortex ripples are presented. Tests were carried out for oscillatory flows, a pure wave, steady currents and a wave plus co-directional currents. PIV generates instantaneous, full-field velocity data and as such is ideal for studying the step-by-step evolution of complex flows. The fine grid of data points in each velocity field is used to derive vorticity data. Both velocity vector maps and vorticity plots are presented. Velocity profiles are obtained and used to calculate physical and apparent roughnesses and friction velocities. The trajectories, circulations and radii of the periodically shed vortices are determined and compared to the predictions of a discrete-vortex model with good agreement within the limitations of the model.

Declaration

This thesis has been composed by me and, except where stated, the work contained is my own.

Heather Earnshaw

November 1996

Acknowledgements

I would like to thank the following people for their advice and assistance during this project: my supervisor, Clive Greated, for his guidance throughout, along with Bill Easson; Frank Morris and the rest of the workshop for their technical help; Carsten Lodahl, Mutlu Sumer, Jørgen Fredsøe and the technical staff at ISVA for enabling me to carry out experiments at their institute; Martin Block and Jonathan Malarkey for providing data from their model; Iain Morrison for reading and correcting this thesis without too much sarcasm. I would also like to thank Rona, Ak and Fred for their wit, sagacity and mountains.

This research project was funded by the DENI and the EU MAST programme and their support is gratefully acknowledged.

Contents

Chapter 1

Introduction

1.1 Subject Background

It is now widely accepted that knowledge of the flow and sediment transport over sea-beds is vital in relation to topics such as erosion, surface wave dissipation and pollution dispersion. Flow patterns over a flat, smooth bed are now well understood. Unfortunately, sea-beds are rarely flat. In coastal areas, where an ability to predict onshore-offshore sediment transport is crucial in determining whether a beach will erode or build up, the sea-beds tend to be 'rippled'. These quasi-steady, two dimensional bed forms, of the order of 10 cm long (crest to crest) and 1 cm high (trough to crest), lie in parallel lines across the direction of the waves as illustrated in fig. 1.1. They can also be found on deep sea bottoms during storms [52]. There is still a lack of knowledge regarding the exact influence of bed geometry on the flow of water above the bed.

The waves at the water surface induce horizontal oscillations at the bed. In

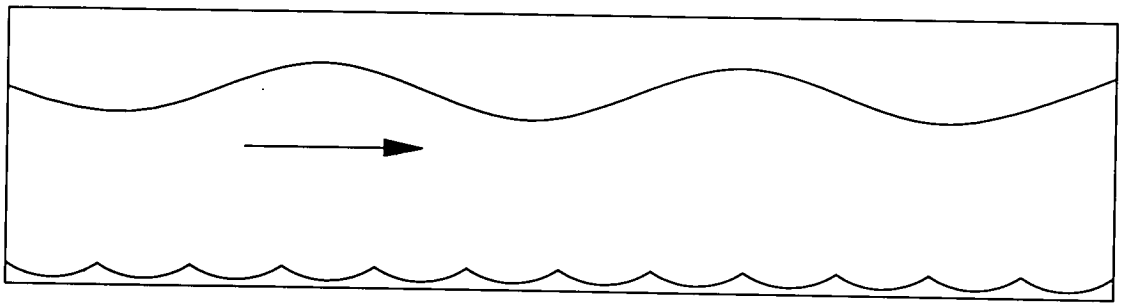

Figure 1.1. Surface waves moving over a rippled sandy bed.

the first half-cycle of an oscillation over a ripple, a vortex is formed on the ripple's lee-side, picking up sand particles, fig. 1.2. At the end of the half-cycle, the flow direction reverses, the vortex is lifted up, over the crest and is carried some distance away depending on the prevailing wave and current direction. The sand grains are released as the vortex decays through viscous effects. Meanwhile, the flow having now reversed, a new, counter-rotating, vortex is formed on the opposite side of the ripple. It in turn picks up sediment and is shed from the ripple. The vortices tend to scoop sand from the troughs of the ripples and deposit it at the crest of another ripple further along, thus repairing the erosion from the flow over the crests. The result is a surprisingly stable ripple pattern with a net sediment drift.

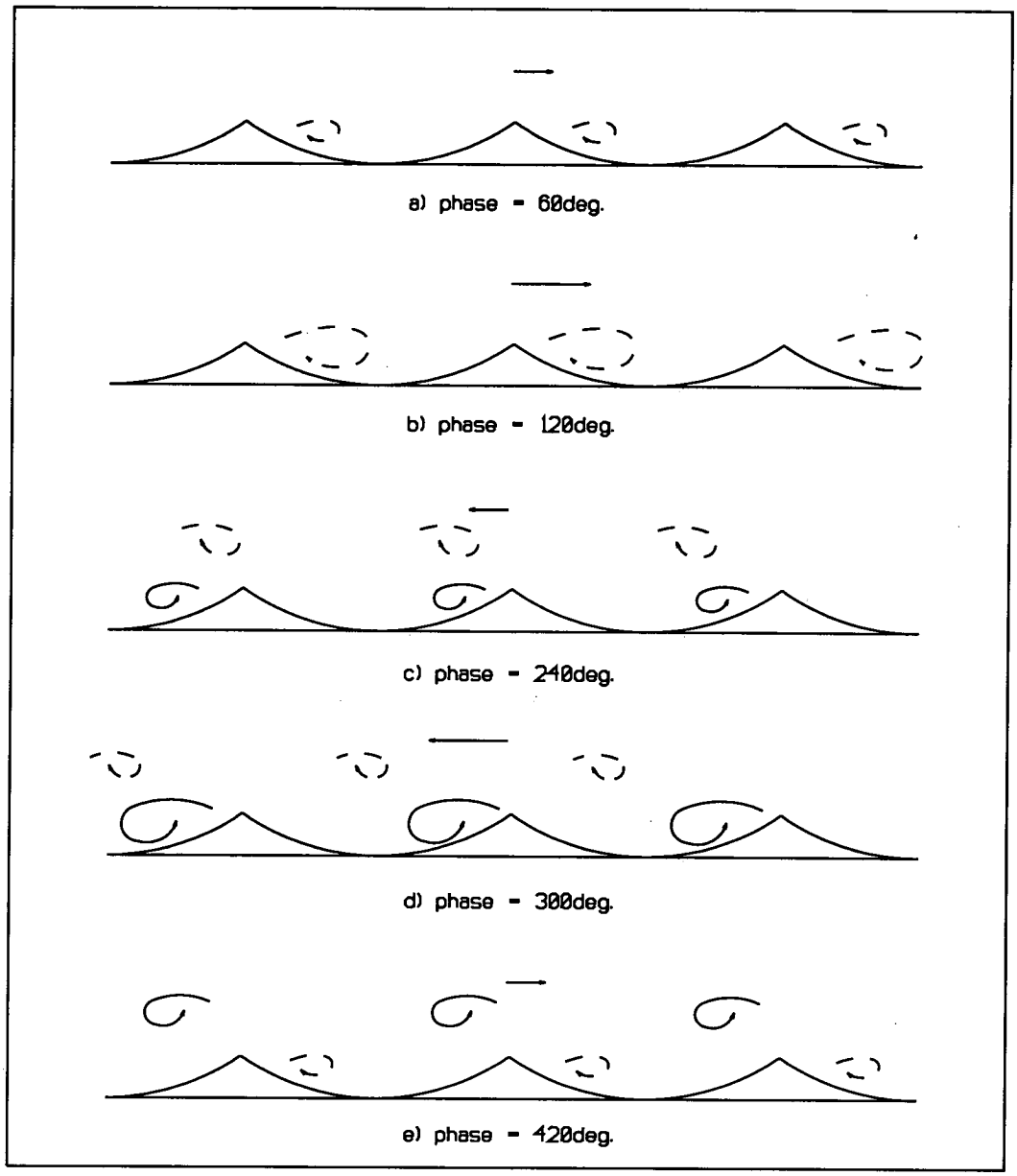

Figure 1.2. A schematic diagram to illustrate the sequence of vortex shedding. Phases and vortex sizes are approximate. The size and sense of the arrows indicate flow strength and direction. a), b) As the flow accelerates from left to right in the first half-cycle, a vortex forms on the lee-side of the ripple. c), d) After flow reversal, the negative (clockwise) vortex has been shed and dissipates while travelling over the ripple while a new, growing, positive (anti-clockwise) vortex forms.

The processes by which ripples are formed, their shape and the limiting factors in their size are known and described by Sleath, Nielsen and Broker [53, 44, 8], for example, but the quantitative details of the resultant flow patterns are not so well understood. In order to predict sediment transport, wave attenuation and dispersion of pollution, these details need to be resolved.

There are two mechanisms involved in the movement of sediment: its entrainment in growing vortices at the bed and its subsequent convection within the vortex and release along the bed. These need to be better understood. Wave energy will be lost during the creation of the ripples and thereafter throughout the vortex-shedding process. Tunstall and Inman [57] found that the vortices accounted for about 7% of the measured wave energy loss while Sleath [53] suggests that for steeper ripples (a ratio of ripple height to length, η/λ, greater than about 0.16) this value might be higher. The remaining energy loss is assumed to be due to absorption by bottom shear. Bagnold [3] showed that the drag coefficient, C_D, from a rippled bed is of the order of 10^{-1}, where C_D is defined by him in terms of mean drag per unit area, D, angular speed of his oscillating tray, ω, and amplitude of oscillation, a, as $C_D = D/\rho\omega^2 a^2$. This value is two orders of magnitude greater than for a flat bed, which will have a huge effect on wave energy dissipation. So in order to predict wave height attenuation, the details of forces and stresses on the ripples due to the flow must also be understood and predictable.

Since Bagnold's [3] early work in 1946, numerous researchers have performed experiments on rippled beds. Until the early 1980s, as summarised by Du Toit

and Sleath [12], few of these investigations studied realistic ripples. Over the last fifteen or so years, numerous people including Du Toit and Sleath, Sato et al, Horikawa and Ikeda and Ranasoma and Sleath [12, 49, 24, 47] have carried out velocity measurements over a wide variety of more realistic cases. These have produced many useful measurements of the time-averaged components of the flows. One of the main points of interest, however, is the growth, transport and decay of the vortices. It is impossible to determine this complex life-cycle of vorticity from the coarse grid of time-averaged velocity measurements yielded by point-measurement techniques.

Over the same period, methods for calculating the flow have also developed extensively. As summarised again by Du Toit and Sleath [12], numerical models have evolved from treating the ripples as roughness elements and thus extending solutions for turbulent flows over rough boundaries. There was the realisation that the momentum exchange might be dominated by mixing from the vortices rather than from smaller-scale turbulent eddies. Then there was the advent of more sophisticated methods such as the 'discrete vortex' model proposed by Longuet-Higgins [39]. A direct numerical calculation of oscillatory flow over a wavy bed generally needs too much CPU (central processing unit) time, although Blondeaux and Vittori [6, 59, 7] have carried out such calculations. (Simulations over a wavy bed may be a precursor to solutions for sharper, steeper ripples.) More recently, the discrete vortex model has been further developed by various researchers and other approaches have been tried. These are well summarised by Davies and Villaret [10] and some are compared in Lewis et al [36]. The current abundance of models needs time-stepping details of the development of the flow

and the vortices to validate their predictions. The aim of this work has been to provide this data.

1.2 Study of wave and wave plus current flows over ripples

1.2.1 Experiments

This study was largely carried out under the auspices of the EU sponsored Marine Science and Technology (MAST-II G8-M) programme: a European collaboration on coastal morphodynamics. Therefore the measurement domain was, to a certain extent, dictated by the demands of different experimentalists and modellers trying to find an area of overlap to enable direct comparison of results. This area was inevitably fairly small. Experimentalists had very different set-ups and measurement techniques while modellers had different approaches and made different assumptions about the flows. Experiments were confined to pure waves or oscillations; three amplitudes of oscillation were to be studied. The parameters have been extended in this work to include a steady flow component in some of the tests. The ripples themselves were solid rather than mobile; the intention was to study the flow not the sediment.

1.2.2 Measurement technique

Particle Image Velocimetry (PIV) is a relatively new velocity measurement technique. Photographs of a stroboscopically illuminated, seeded flow are used to

determine the instantaneous velocity at every point in the flow. It is thus non-intrusive and gives simultaneous full-field data [1, 31]. As implied earlier it is the latter ability which makes this work novel. Over the last ten years a great deal of expertise in PIV has been built up at the University of Edinburgh, initially by Gray and Skyner [20, 51]. A few of the numerous examples of the applications are given in Bruce and Easson, Morrison and Greated and Earnshaw et al [9, 43, 13].

Although each photograph is taken in an instant, developing the film and analysing the negatives is time consuming. The analysis rig used took approximately 2 seconds per point which for a grid of about 50 by 35 points translates into about one hour per negative. This one negative yields a very close-packed grid of data points for one instant in the flow. This is the advantage of PIV compared to point measurement techniques such as laser doppler anemometry, LDA, which give time averaged measurements at relatively few points. Thus LDA data can be used to find turbulence characteristics such as Reynolds Stresses at a few points while PIV enables a study of step-by-step evolution of the flow. As high speed, high-resolution video cameras are becoming a more realistic proposition, PIV will move towards much faster data acquisition and this dilemma between temporal and spatial resolution will be removed.

1.3 Thesis content

After a discussion of ripples in general, descriptions of the theories, methods and facilities used in this investigation are given. Two sets of results are then presented. Firstly, flows without a steady component were considered. These were of two types: oscillations in a towing tank and waves in a wave flume. Then steady flows were introduced. The flows were measured first with the currents alone over the ripples and then with the same currents combined with the wave studied in the previous chapter. Velocity measurements of all these cases were made at several phases of the wave-cycle using PIV.

The two main aspects of the flow, the characteristics of the boundary layers and the process of vortex formation and shedding, could then be further investigated from this velocity data. Velocity profiles were used to determine boundary layer thicknesses, the friction velocities and roughness parameters as appropriate. Four vortex characteristics — circulation, radius, and $x-y$ co-ordinates of the vortex centre — were derived at each time-step throughout each of the flows. For the wave/oscillation cases they were compared with the predictions of a discrete vortex model developed at the University of Wales, Bangor.

Chapter 2

Ripples

2.1 Summary

This short chapter gives some further background to ripples in general: how and where they occur and what factors determine their size and shape. The particular ripple used in these experiments is also specified.

2.2 Ripples

Sandy sea beds tend only to be flat either when the water above them is stationary (though even then, relic ripples formed by earlier fluid motion may not have been destroyed) or alternatively in regions of very high velocity and therefore a very high sediment transport rate where the ripples disappear and sheet flow emerges. In areas of low to moderate sediment transport rates the sea bed will be covered by bed forms. Fine sediment tends to form into ripples, with lengths

(crest to crest, λ) up to about 60 cm and heights (trough to crest, η) up to 6 cm; coarser sediment tends to produce dunes. Generally, a ripple pattern will start to form once the fluid velocity has passed the critical value for initial sediment movement. This value depends on the sediment grain size and on the density of both the fluid and the sediment.

Consider first oscillatory motion over an already slightly wavy bed. Once sand begins to be moved back and forth over the bed, streamlines such as those in fig. 2.1 are set up in the time-averaged flow [53]. At the bed these recirculating cells tend to carry sediment up towards the crests, away from the troughs. Thus the ripples will grow. While both the forward and reverse flows tend to carry sediment up towards the crests from the troughs, gravity tends to move the sediment back into the troughs. Once a ripple pattern has started to form, its shape will be reinforced by the flow but as the ripples get higher and steeper, gravity has an increasing influence on the sand grains and therefore the ripples have a limiting steepness. So from an initial slight 'wave' on the bed a well-defined ripple pattern forms. It can be shown [53] that the same processes will cause a ripple pattern to start at and spread out from any obstacle or large pebble or even just a few grains of sediment piled up.

Bagnold [3] distinguished two types of ripple, a rolling-grain ripple and a vortex ripple. It has been suggested by Sleath and Nielsen [53, 44] amongst others that the so-called rolling-grain ripples must form first. These have relatively gentle slopes. If the ripples continue to grow they get so steep ($\eta/\lambda > 0.1$) that the flow separates behind the crest at the end of each half-cycle and vortices are

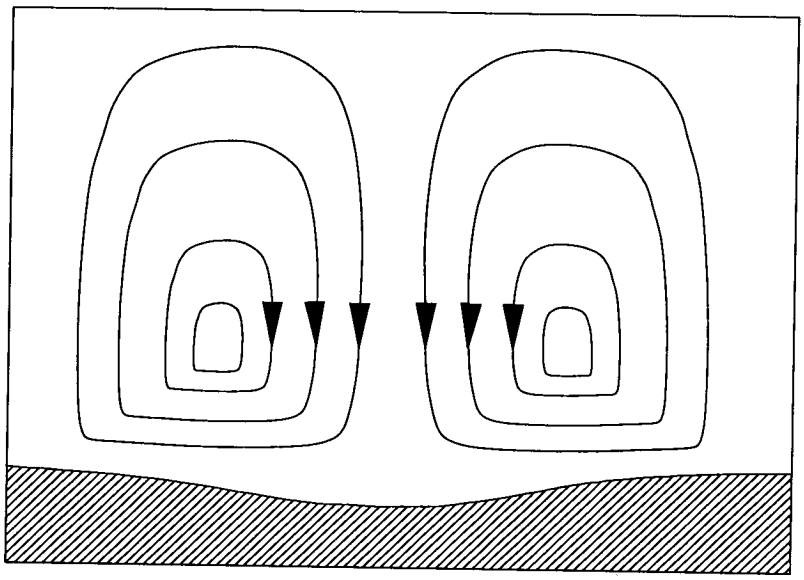

Figure 2.1. Streamlines of the mean flow over a wavy bed.

formed. These ripples are known as vortex ripples. As soon as a rolling-grain ripple has become steep enough for flow-separation to occur, the ensuing vortices pick up sand grains from within the ripple troughs and after ejection from the bed, carry the sediment along the bed. Thus the wavelength, λ, of the ripples is no longer solely a function of the amplitude of oscillation, a, of the fluid and the pattern changes. Bagnold observed that *"the new regime of vortex ripples spreads rapidly over the rest of the surface like a disease"*. Vortex ripples are larger than and have a slightly different profile to the rolling-grain ripples. It is the vortices which are responsible for the high sediment transport rates and therefore the steeper ripples are of more interest. Hereafter 'ripples' will be assumed to refer to vortex ripples.

Once formed, these ripples are nearly steady. During each half cycle the sediment at the crest is moved slightly downstream making the crest flatter upstream fig. 2.2. This alternates on either side of the ripple as the flow reverses. However, the amount of sediment moved in this way is minimal compared to the volume of sediment in the bed form as a whole, so the ripples are regarded as steady. The sediment transport of interest is a direct result of the vortices formed and shed during each half-cycle.

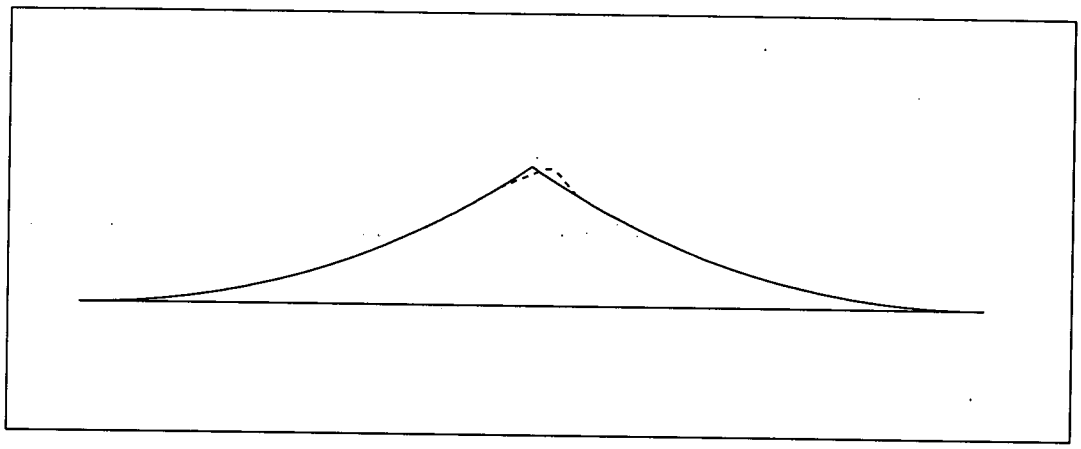

Figure 2.2. The difference between the mean (solid line) and instantaneous (dashed line) ripple profile. (Partly after Sleath [53])

A number of researchers (for example Bagnold and Nielsen [3, 44, 45]) have tried to find means of predicting ripple parameters for a given flow. Vortex ripples are generally two-dimensional though occasionally a 3-D 'brick' pattern forms [3, 60] if the amplitude of oscillation, a, is small. They have a well defined range of steepness, $0.1 < \eta/\lambda < 0.25$. Ripple length, λ, has been found to depend strongly on the amplitude of oscillation, a, ($a/\lambda \approx 2/3$) especially at lower rates of sediment transport. At higher rates, the ejected vortex carries a considerable

amount of sediment and the ripple length will be influenced by the position along the bed at which this sediment is released. At values of a/λ less than about 0.4 the oscillations are too small for vortices to form. Perhaps surprisingly, the size and density of the sediment do not greatly affect ripple dimensions [53] and nor does the water depth [17]. The influence of Reynold's number, Re, is weak. (Reynold's number is defined as $Re = U_0 a/\nu$ where U_0 is the amplitude of the free stream velocity and ν is the kinematic viscosity.) Further details are given by Sleath [53]

The above description assumes a symmetric flow. That is the free stream flow is oscillatory so the forward and reverse flows and therefore the two recirculating cells are identical. If instead there is a steady current, then the ripple profile will be asymmetric, fig. 2.3. Similarly in a combined wave and current flow the geometry will depend on the relative strengths of the two flow components. The ripples will become more asymmetric with increasing current for a given wave but there seems to be little change in η or λ [53].

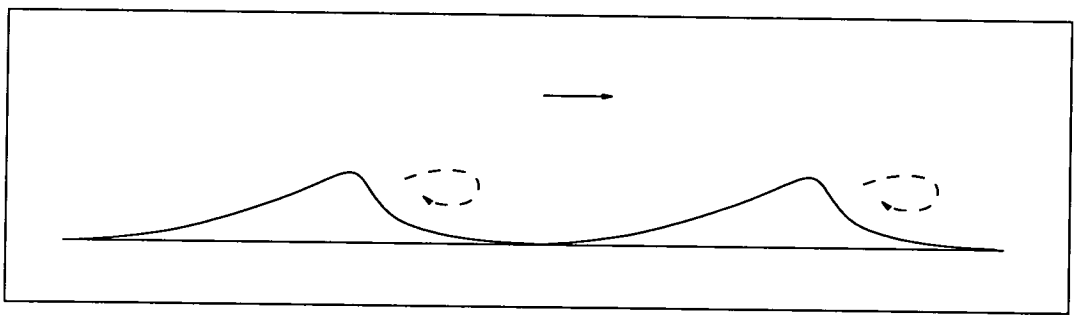

Figure 2.3. An asymmetric ripple. The lee slope is steeper and the upstream slope more gentle than for a symmetric ripple.

2.3 Experimental ripple parameters

The ripples used in the experiments described here were solid and pre-formed from styrofoam. The intention was to study directly the fluid flow around the ripples rather than the resultant sediment motion. For PIV measurements (unless some kind of two-phase measurements were made) this meant using solid ripples. For a given flow, the ripples do stabilise to a particular form so as long as suitable parameters are chosen the experiments should still be realistic. Some asymmetry in the ripple profile might be expected in the current and wave plus current flows. However, it was decided to use the same ripple shape under all the flows to make a comparison of the effects of the presence of ripples on the different flows easier.

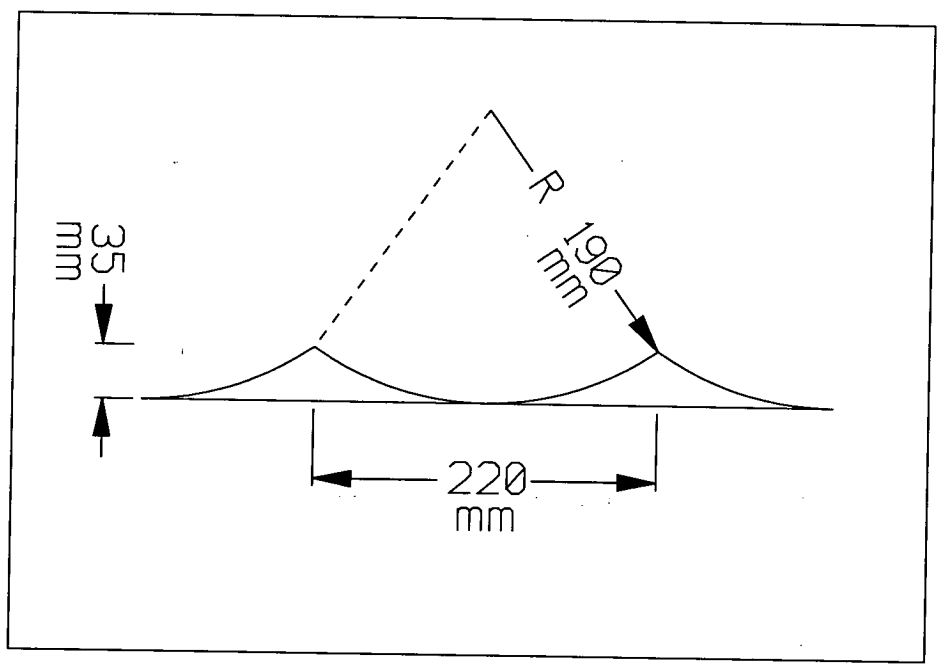

Figure 2.4. Dimensions of MAST standard ripple: length, $\lambda = 22$ cm, height, $\eta = 35$ mm.

The EU MAST G8-M programme agreed on a 'standard' ripple shape and size. This is a sharp crested ripple, $\lambda = 22$ cm and $\eta = 35$ mm. The ripple shape was approximated to an arc of radius 19 cm as shown in fig. 2.4. The crest was sharp, rather than a more realistic rounded shape, to make fixing a point of separation easier for the numerical modellers in the group. The main difference predicted by Horikawa and Mizutani [25] is that sharp crests might produce larger vortices than round crests.

Chapter 3

Experimental facilities and techniques

3.1 Summary

All the velocity measurements described here were carried out using the relatively new technique of Particle Image Velocimetry (PIV). To resolve these flows fully it was also necessary to incorporate image shifting. Two different methods were used. The earlier tests used the simplistic approach of panning the camera during exposure. Later a rotating mirror system was used. Two tanks were used; a towing tank for the oscillatory tests and a wave flume for the wave and current flows. To achieve oscillatory motion, the ripple bed was suspended upside down in the tank from a computer controlled trolley which was programmed to move back and forth.

3.2 Particle Image Velocimetry (PIV)

All the measurements were made with the PIV system developed in the University of Edinburgh Fluids Group by Gray and Skyner [20, 51]. PIV is still a relatively new technique so a brief general summary will be given. An in-depth description is not deemed appropriate here. Further discussions are given by Adrian and Gray [1, 21]. A more detailed description of the specific set-ups used is given.

3.2.1 PIV method

PIV is a non-intrusive method which gives simultaneous full-field velocity data. The flow is seeded with small, neutrally buoyant particles which scatter light and follow the flow accurately. A pseudo light-sheet 1 m wide and approximately 2 mm thick is generated in the middle of the tank using a scanning beam illumination system [23]. As shown in fig. 3.1 and described in Gray et al [23] the cw (continuous wave) laser beam enters the scanning box, is deflected upwards by a mirror to hit a rotating, octagonal mirror so the beam scans across the parabolic mirror which collimates it into a parallel sheet directed into the tank. Thus the flow is illuminated stroboscopically.

The area of interest is then photographed with a long enough film exposure to ensure that multiple images of the seeding particles are captured on the negative. By measuring the separations of successive images of each particle a full field plot of the velocity at each point in the flow can be built up. The photograph in fig. 3.2 shows the ripples, light sheet, camera and scanning box under the tank.

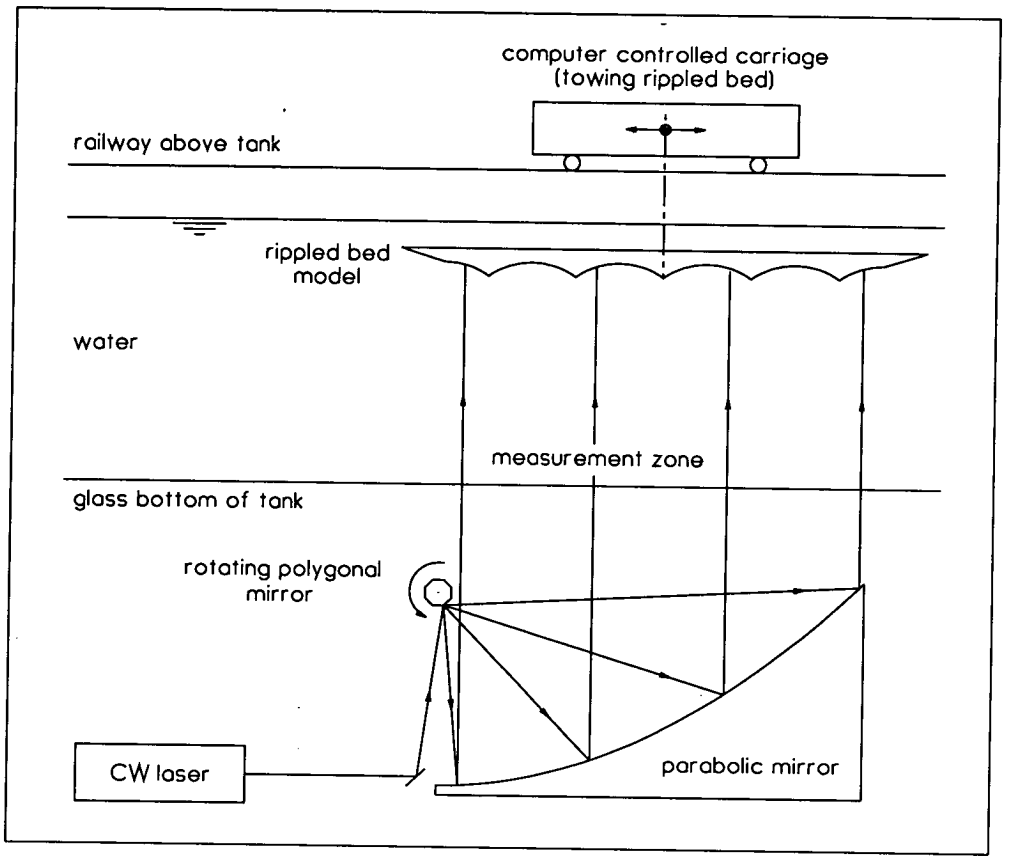

Figure 3.1. The ripple bed attached to the trolley above the towing tank with the scanning beam system under it. (Ripples not to scale.)

By taking a photograph, the velocities over a large area can be studied simultaneously and a detailed knowledge of the flow produced very quickly. There is no intrusion into the flow and therefore no interference with the flow. Nor is there the same reliance on experimental repeatability which there must be in point measurement methods such as LDA which need hundreds of measurements where PIV needs just a few. PIV gives very precise measurements, generally accurate to within a few percent as discussed further below.

The seeding particles in all cases were conifer pollen which have a mean diameter of 70 μm. When wet they are almost neutrally buoyant [46] and follow the flow [20]. Magnification is defined here as the ratio of the length of the image of an object on the film negative to the length of the object. It is found accurately by photographing a grid held in the light sheet and then measuring the size of the image grid using a travelling microscope. Magnifications here were of the order 0.15.

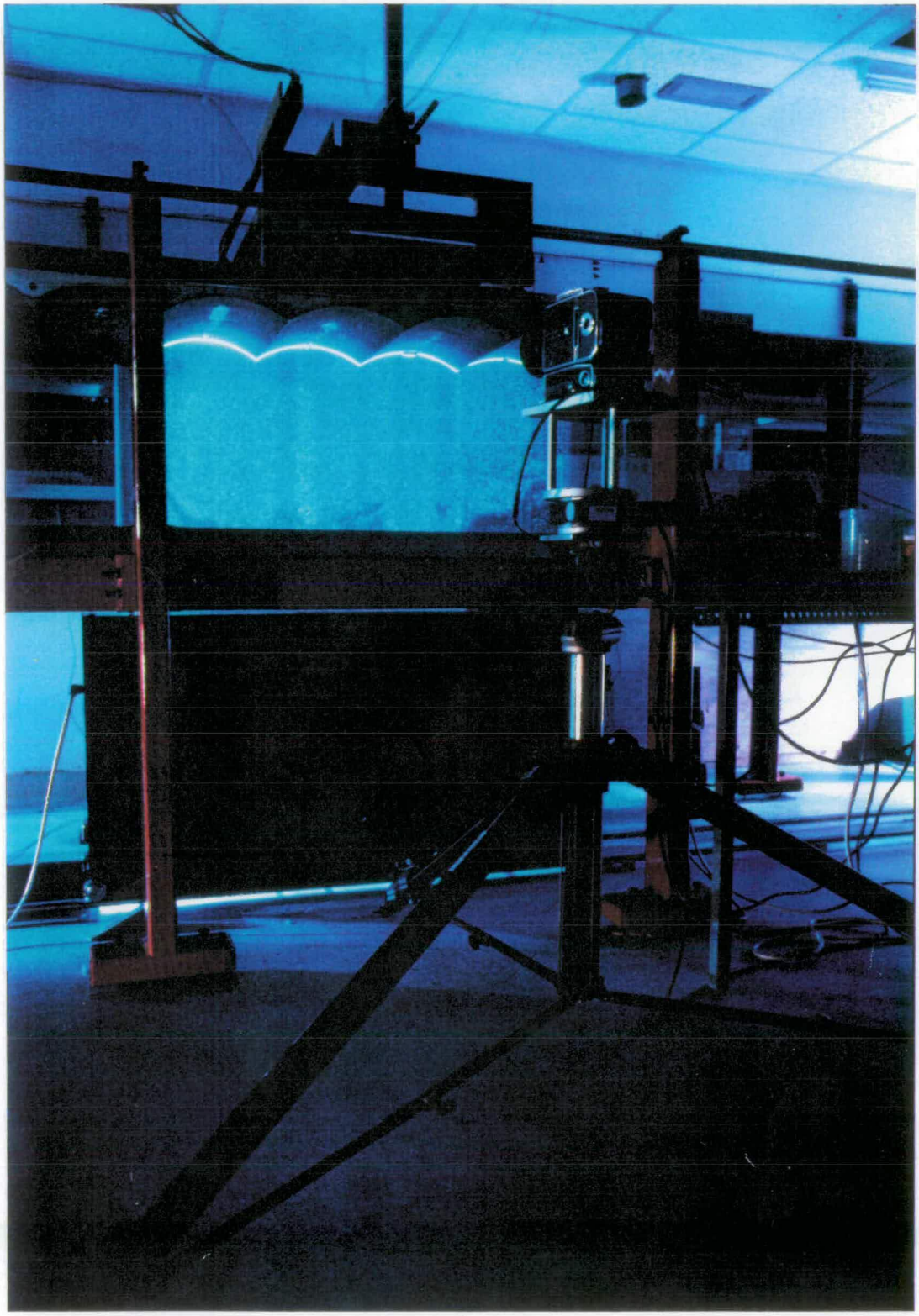

Figure 3.2. The ripple bed model upside down in the towing tank, illuminated by the scanning laser light sheet. The camera is mounted on the image shifting turntable.

3.2.2 PIV analysis

The basic principle of PIV analysis is to measure the separation of successive images of an individual particle. This distance and the known scan time then give the velocity of that particle. In practice it is done less laboriously by dividing the negative into squares ("interrogation areas") and assuming that each particle in that square has the same velocity; a reasonable assumption everywhere except in areas with a very high velocity gradient such as within a vortex. An autocorrelation is performed of every particle image with every other particle image in the same interrogation area, thus allowing the average particle displacement in that area to be found.

It can be shown that the autocorrelation $A(x, y)$ of the intensity distribution $a(x, y)$ across the interrogation area is given by:

$$A(x,y) = \iint a(x,y)\, a(x-x', y-y')\, dx'\, dy' \tag{3.1}$$

and can be calculated using Fourier transform pairs as:

$$A(x,y) = FT^{-1}([FT(a(x,y))]^2) \tag{3.2}$$

The analysis rig developed in Edinburgh by Gray and Skyner [20, 51] performs the first Fourier transform optically and the second one numerically. A low powered (1 mW) HeNe laser probes each interrogation area in turn. The trains of particle images diffract the light and hence produce a Young's fringe pattern (the result of the first FT). The spacing between the fringes is inversely proportional

to the average particle image displacement in that interrogation area and the direction of the fringes is perpendicular to the direction of the flow. The pattern is recorded digitally by a CCD (charge coupled device) camera. The camera senses and records the intensity of the fringe pattern so the first FT is automatically squared. The second FT is then carried out by the PC using a 2-D fast Fourier transform algorithm. This and the movement of the translation stage are the most time-consuming parts of the whole analysis procedure; the first two stages being almost instantaneous. In this study one point took approximately two seconds to analyse so a grid of 50 by 35 points took about an hour. The PC finds and removes the largest peak which should correspond to the correlation of each image particle with itself and therefore does not contain any relevant information. It then locates the two secondary peaks, corresponding to the correlation of each image particle with itself one time-step later and finds the spacing and relative orientation between them, thus giving speed and direction of the flow at that point. The direction found by this method has an inherent 180° ambiguity. The analysis system assumes the horizontal velocity to always be positive. In simple unidirectional flows this is not a problem, the whole field can be aligned to the known direction as necessary. In more complicated flows, where there may be flow reversal, this causes more serious problems which will be discussed further in section 3.3.

Having acquired a velocity map the final stage is manual editing. There will inevitably be spurious vectors where the ripple bed was, at the edge of the frame or in areas where the seeding density was too low, or too high, or dirt in the flow got into the light sheet. The last few examples can usually be limited to a

certain extent but are difficult to eliminate altogether. It would be very difficult to automate this editing stage but the obvious discontinuities mean that it is usually relatively easy to spot 'bad' vectors by eye.

3.2.3 PIV accuracy

The accuracy and reliability of PIV as a measurement technique have been extensively discussed in the literature so only a brief summary of the main points of concern is given here. In particular, Gray and Quinn [20, 46] have both discussed the accuracy of PIV and found errors in the velocity measurements to be of the order of a few percent at worst. The errors can be divided into random and systematic.

Random errors

The first sources of random errors are due to a reliance on the experimenter to align the camera and image shifter with the tank, measure the magnification (defined above) and the laser beam scan rate and to focus the camera. These errors can be dramatically reduced by being painstakingly careful when setting up the experiment.

The illumination plane must be kept as narrow as possible, ideally about 2 mm thick at the water surface. While the laser beam is steered optically from the

laser to the measurement area, the beam expands and must therefore be recollimated at the scanning box. It is impossible to totally recollimate the laser beam so the sheet inevitably thickens as the beam travels upwards through the water. If it becomes too thick, too many particles are illuminated with, individually, less light. This leads to an increase in background noise during analysis. However, by taking care with the collimating optics and the alignment of the laser beam and keeping all the optics as clean as possible this problem too can be minimised.

During the analysis, there will always be some random correlation noise due to correlations between unrelated particles. This is inevitable. Hence there is always some slight uncertainty in detecting the centres of the correlation peaks. The only way to reduce this is by producing high quality PIV negatives.

Systematic errors

The changes in refractive index at the air-glass-water interface cause errors in determining the position and displacement of each seeding particle. These errors are more difficult to eliminate. The error introduced by the interface is due to the non-linearity in the law of refraction (Snell's Law). The absolute values of position will not be shifted in the centre of the negative but will get progressively inaccurate further from the optical axis, the error rising rapidly at the edges. To reduce the effect of this, photographs were taken of a wider field than was required. Data at the edges of the negative, while being useful in establishing the overall qualitative picture of vortex trajectories, were not used in any calculations. The ripple crest, as near as possible, was in the centre of the field of

view, so the maximum error will always be at the troughs. From curves found by Jakobsen [27], this maximum error in the oscillating experiments is ± 1.5 mm, compared to a ripple length of 220 mm. In the wave plus current experiments, where magnification was less, so a smaller portion of the negative is used, this error was reduced to ± 0.6 mm. The effect is non-linear and therefore difficult to correct for. In the worst case, the error in the position is less than 1% of the ripple length which is within the total error for PIV. Moreover, Gray [20] showed that another systematic error due to the lens aberration almost exactly counteracts that due to refraction.

There are further systematic errors due to, for example, the analysis rig calibration; the seeding particles having a slight tendency to rise; there will be some distortion of the illumination plane due to the problems of fabricating a perfect parabola; exact scan times will vary for individual particles depending on their direction of motion compared to the movement of the scanning beam. Quinn [46] gives more details about all of these and quotes a combined error of around 2.0% relative to the maximum velocity in the flow. To keep errors as low as possible it is well worth using a good camera, good film and so on. A Hasselblad 500 EL/M with a flat-field 80 mm lens and Kodak TMAX 400 film were used.

To summarise, PIV although quite simple in concept is more complicated to put into practice and is very time-consuming. It does however, with care, yield accurate data.

3.3 Image shifting

In oscillating flows, two measurement difficulties arise when using PIV. Directional ambiguity occurs because there is no way of telling which of the particle multiple images came first and near-zero velocities cannot be measured as the images are too close together to be discriminated by the analysis system. To overcome these two problems the technique of image shifting [2] was used. This superimposes a known shift velocity onto the flow field such that the subsequent images always occur on the same side of the first particle image, resolving the problem of directional ambiguity. In addition to this the areas in the flow with near-zero velocities now have an apparent, measurable velocity. This technique is analogous to frequency shifting in LDA. The simplest way of including a shift velocity is to move the camera during the exposure. This was achieved in the first experiments by mounting the camera on a computer controlled turntable. The shutter is triggered when the optical axis of the camera is perpendicular to the tank [9]. Later this was replaced by a more sophisticated rotating mirror system, whereby a mirror held vertically in front of and at 45° to the camera rotates about its cental vertical axis during exposure [42]. Note that the camera or mirror is moved appropriately to tie in with whichever phase is required. In both cases the shift velocity is subtracted from the analysed negative to reveal the true flow field.

3.3.1 Errors due to image shifting

The addition of another set of equipment inevitably leads to new sources of both random and systematic errors even apart from having more equipment to align

accurately. The turntable speed may be slightly variable from one frame to the next or even within the same frame. The rotation may vibrate the camera, especially in the first system used where the whole camera is moving, or the mirror in the rotating mirror system. These random errors can be reduced by using high quality turntables and taking time to set up the experiment carefully.

Some of the systematic errors are more difficult to eliminate. Problems arise because the negative sees a changing field of view as the camera, or mirror, rotates during exposure. The shift velocity, usually assumed to be constant across the measurement area, will vary if the shift is achieved using some form of rotation. In the rotating camera case, the camera is looking at and photographing a flat plane while moving in an arc, so points at the edges of the negative are given a greater shift than those in the centre. Similarly for the rotating mirror. The error is zero on the optical axis, at the centre of the photographic negative and increases non-linearly towards the edges of the field of view. This effect will be greater the closer the camera is to the measurement plane. Morrison [42] showed that it may cause the horizontal component of the shift velocity to vary by up to 10% at the extremes of the negative. He also describes the variation in the vertical component which is much more difficult to quantify.

The effect was first noticed on the velocity field maps from the oscillatory experiments. The increased velocities are evident in the upper corners of fig. 5.1. However, the ripple crest was always near the centre of the field of view where this error is smallest and the bulk of the analysis of the oscillatory tests is concerned with the vortices which do not travel vertically very high. By photographing

wider than one ripple length, the field could be cropped before analysis and the horizontal distortion reduced in the area of interest. Thus it was decided that as the increase in the overall error would be negligible in the areas of interest those tests would not be repeated.

For the later wave and current experiments the effect was corrected for. The obvious method was by using shift calibration pictures: several photographs of still water were taken using the required shift velocity, the ensemble average of those pictures was found and then that vector map was subtracted from the data maps.

Thus the technique of image shifting was successfully implemented to allow these complicated flows to be fully resolved, even in areas with reverse flows.

3.4 Flumes

Two different tanks were used for these experiments. The oscillatory work was carried out in a towing tank in Edinburgh but the tests which included a steady flow component needed more space so they were carried out in a larger wave plus current flume at the Institute of Hydrodynamics and Hydraulic Engineering (ISVA), Technical University of Denmark. These two facilities are described below.

3.4.1 Towing tank

Flow near the bed is in general oscillatory [54] so studies of these regions are frequently carried out in oscillating water columns or with oscillating beds [47, 49]. Edinburgh's towing tank is six metres long, a metre wide and for these tests was filled to a depth of half a metre. The sides and base of the tank are glass to give as much versatile optical access as possible. It is easiest to have the light sheet entering from underneath the tank and to suspend the ripples above the tank, as shown in fig. 3.1. The phenomenon of hydrostatic balance means that inverting the flow is perfectly acceptable [56].

Rather than using an oscillatory flow over stationary ripples the ripple bed was oscillated within the flume. The two are not obviously identical as the frames are accelerating. Tritton and Garrison [55, 18] both show that they are. In particular, Tritton shows that the equations of motion in the oscillating frame can be put into the same form as those in the inertial frame. He starts with the incompressible Navier Stokes and continuity equations:

$$\frac{\partial u_i}{\partial t} + u_j \frac{\partial u_i}{\partial x_j} = -\frac{1}{\rho}\frac{\partial p}{\partial x_i} + \nu \frac{\partial^2 u_i}{\partial x_j^2}, \tag{3.3}$$

$$\frac{\partial u_j}{\partial x_j} = 0, \tag{3.4}$$

where $x_i = (x_1, x_2, x_3)$ are the co-ordinates in the inertial frame. In the non-inertial frame, (x_1', x_2', x_3') oscillate relative to the inertial frame such that $x_1' = x_1 - a\sin\omega t$, $x_2' = x_2$, $x_3' = x_3$ and $t' = t$.

$$\frac{\partial f}{\partial x} = \frac{\partial f}{\partial x'}\frac{\partial x'}{\partial x} + \frac{\partial f}{\partial t'}\frac{\partial t'}{\partial x} = \frac{\partial f}{\partial x'} \tag{3.5}$$

and

$$\frac{\partial f}{\partial t} = \frac{\partial f}{\partial x'}\frac{\partial x'}{\partial t} + \frac{\partial f}{\partial t'}\frac{\partial t'}{\partial t} = \frac{\partial f}{\partial t'} - a\omega\cos\omega t\frac{\partial f}{\partial x'}. \tag{3.6}$$

Hence eqns. 3.3 and 3.4 become:

$$\frac{\partial u_i}{\partial t'} - a\omega\cos\omega t\frac{\partial u_i}{\partial x'} + u_j\frac{\partial u_i}{\partial x'_j} = -\frac{1}{\rho}\frac{\partial p}{\partial x'_i} + \nu\frac{\partial^2 u_i}{\partial x'^2_j}, \tag{3.7}$$

$$\frac{\partial u_j}{\partial x'_j} = 0. \tag{3.8}$$

The origin of the non-inertial frame moves with velocity $(a\omega\cos\omega t, 0, 0)$, hence $u'_1 = u_1 - a\omega\cos\omega t$, $u'_2 = u_2$ and $u'_3 = u_3$. Substituting these into eqns. 3.7 and 3.8 gives:

$$\begin{aligned} -\frac{1}{\rho}\frac{\partial p}{\partial x'_i} + \nu\frac{\partial^2 u'_i}{\partial x'^2_j} &= \frac{\partial u'_i}{\partial t'} - a\omega^2\sin\omega t'\delta_{i1} - a\omega\cos\omega t'\frac{\partial u'_i}{\partial x'} + \\ &\quad u'_j\frac{\partial u'_i}{\partial x'_j} + a\omega\cos\omega t'\frac{\partial u'_i}{\partial x'_j}\delta_{j1}, \end{aligned} \tag{3.9}$$

$$\frac{\partial u'_j}{\partial x'_j} = 0, \tag{3.10}$$

where

$$\delta_{i1} = \begin{cases} 1 & \text{if } i = 1 \\ 0 & \text{if } i \neq 1. \end{cases}$$

As $p' = p - \rho a\omega^2 x \sin\omega t'$, then:

$$\frac{\partial u_i'}{\partial t'} + u_j' \frac{\partial u_i'}{\partial x_j'} = -\frac{1}{\rho}\frac{\partial p'}{\partial x_i'} + \nu \frac{\partial^2 u_i'}{\partial x_j'^2}, \tag{3.11}$$

$$\frac{\partial u_j'}{\partial x_j'} = 0. \tag{3.12}$$

The motion in the non-inertial frame is governed by the same equations as for the inertial frame but with a different pressure field. So the flows are identical. To make the experiments physically easier the ripples were attached upside down to a computer controlled trolley which could then oscillate them in initially still water. The model ripple bed was 6 full ripples long with a 'half-ripple' at either end, tapering at the trough to eliminate edge effects from the ends of the bed.

3.4.2 ISVA wave flume

None of the flumes in Edinburgh has shallow water wave and current facilities so under the MAST programme the tests for this part of the work were carried out at ISVA, Technical University of Denmark. A full set of PIV experimental equipment (including a laser, scanning box, camera and image shifting system) was taken to the ISVA institute in two visits of three weeks each. Whereas the tank in Edinburgh was purpose-built for PIV experiments, no-one had previously carried out PIV tests at ISVA. Thus the system used in Edinburgh had to be adapted to suit their tank and in particular the test section had to be designed and built as described below.

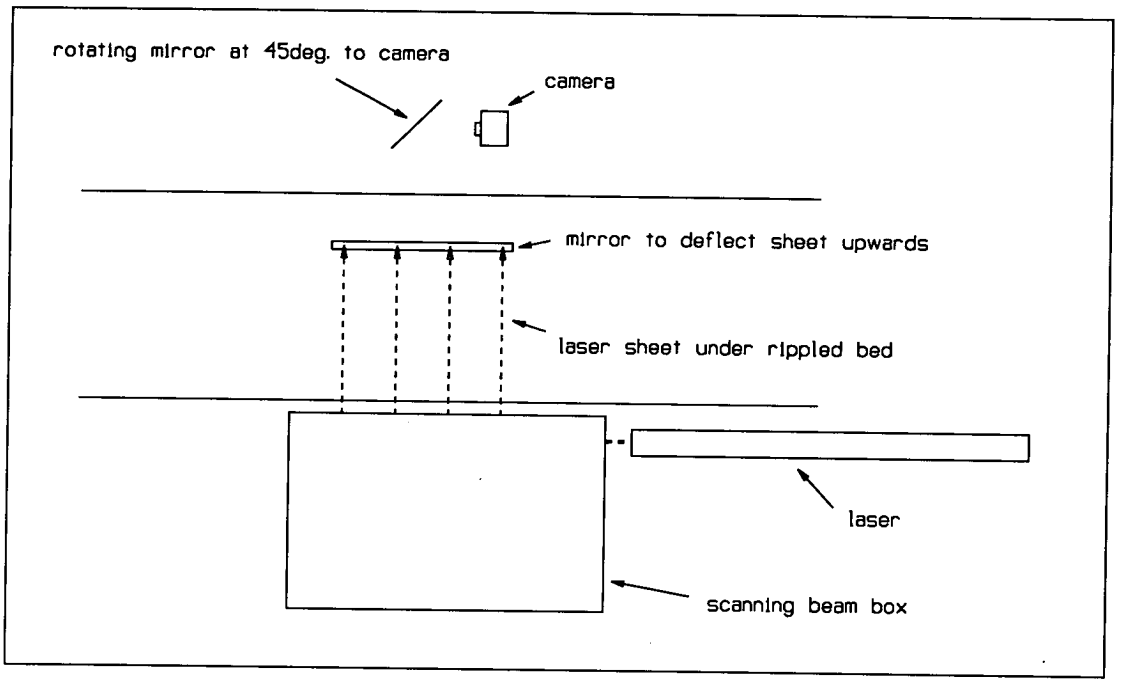

Figure 3.3. Plan view of the layout of apparatus at ISVA

The flume used at ISVA is a wave flume of 28 m x 0.6 m, with a current facility, and was filled to a depth of 0.4 m for these tests. The ripples were the same shape and size as above, moulded in concrete except for the test section which was again formed from styrofoam and situated 15.5m from the wave paddle. The base of the tank is opaque so the scanning box could not sit under the tank as it does in Edinburgh. A section of their concrete rippled bed was replaced with one made in Edinburgh designed so that a light sheet entering the tank horizontally (between the tank and the bed) was deflected upwards by a mirror held at 45°

under a gap in the bed, fig. 3.3. The gap was then covered with a strip of transparent plastic folded around the crests and taped down along the edges. This is a cheap and easy way of allowing optical access but is not without problems. As the tank filled up, air-bubbles collected under the plastic and had to be removed with a syringe. A more serious problem was that the pollen, which has a slight tendency to rise, coated the underside of the strip overnight, between experiments, dramatically reducing the amount of light reaching the measurement area. Some of the pollen could, with care, be removed along with the air bubbles every morning before taking pictures, but the problem was never completely resolved. Emptying the whole tank, replacing the strip and refilling the tank would be the best solution in a smaller facility. This solution was impractical here as the water and hence seeding were recirculated; changing all the water and reseeding would have been too costly. Seeding the flow in the first place was also more difficult in this facility than in the towing tank where the ripples were upside down so that the pollen rising ensured good seeding near the areas of interest. When the ripples were the right way up, forcing pollen down into their troughs was difficult. Secondly, in the towing tank the flow has very little drift, so that with care seeding could be poured along the line of the light sheet and would stay there throughout a test run. However, in the wave flume there was a flow past the measurement point, especially when a current was used, so pollen had to be poured in upstream to provide enough seeding at an appropriate density, even down to the ripple troughs, when the flow took it past the measurement zone. Judging the timings for this, especially for the faster currents, was difficult.

The light sheet was closer (200 mm) to the front of the tank to allow a large

magnification but not so close to the wall that edge effects became a problem. The laser only produced a relatively low power, around 6W. This lack of illumination caused some problems. However, because the laser was adjacent to the tank and its output beam connected directly into the scanning box, thereby eliminating the need for steering optics, the scanning box was smaller (0.5 m rather than 1 m) and the distance from the parabola to the measurement zone was less, there were fewer light losses from laser to camera. Thus the problem was not as disastrous as was at first feared although it is the main cause for some of the data dropouts discussed later.

3.5 Fixing a point of reference

There must be a point of reference on the negative so that appropriate $x-y$ co-ordinates can be fixed onto the analysed data. The most obvious point to choose is the crest of a ripple as it is easily identified on the negative. There are two separate problems associated with fixing this point of reference. The first problem is particular to the towing tank. The ripples are moving relative to the stationary camera (ignoring image shifting for the moment). To ensure that the central ripple crest will be in the centre of the camera's field of view at the right phase of the trolley's oscillation requires very precise positioning of the trolley upstream of the camera before the experiment starts. This also implies that only one phase can be photographed during any one set of oscillations. The trolley must start oscillating further from the camera for successive phases. So the ripple image is unlikely to be exactly in the centre of the negative but can be

close enough to render edge effects extraneous. Thus it is not a serious problem but it does make taking measurements a slightly more laborious process. This is not an issue in the experiments carried out at ISVA's wave flume. The ripples there were fixed, so the camera could be very carefully aligned before any measurements were made such that the central ripple crest was in the centre of its field of view.

The second problem is a direct result of using image shifting. As the camera or mirror moves, the seeding particles are shifted as intended but so too are the ripples; thus there are multiple images of the ripple on each negative. Of these several images, only one will correspond to the 'correct' image where the shifting system was exactly aligned with camera and tank. This image occurs when the camera is perpendicular to the tank for the panning camera system and when the mirror is at 45° to the tank for the rotating mirror system. Only this image will give the exact point of reference, the others will be shifted slightly. The shifting system can be triggered such that the 'linear' position is at the beginning, middle or end of the camera exposure. For all of these measurements, the camera was triggered so that the middle of its exposure occurred when it and the mirror were aligned as required with the tank. Thus the point of reference is the central ripple image.

Test	U_b (m/s)	U_c (m/s)	U_c/U_b	H (cm)	T(s)	a (cm)	a/λ
osc1	0.131				8.46	17.6	0.8
osc2	0.196				8.46	26.4	1.2
osc3	0.294				8.46	39.6	1.8
W	0.28			13	2.5	11.1	0.5
C1		0.10					
C2		0.14					
C3		0.23					
WC1	0.28	0.10	0.36	13	2.5	11.1	0.5
WC2	0.28	0.14	0.50	13	2.5	11.1	0.5
WC3	0.28	0.23	0.82	13	2.5	11.1	0.5

Table 3.1. Parameters of the tests. U_c = mean current velocity, U_b = amplitude of wave velocity, H = wave height, T = time period, a = amplitude of oscillation and λ = ripple length.

3.6 Test parameters

The experimental parameters were initially chosen within the EU MAST G8-M programme to facilitate comparisons between the modellers and experimentalists in the group and were later extended for this study. The test conditions are summarised in table 3.1.

For the oscillatory experiments, three amplitudes of oscillation, a, corresponding to a/λ = 0.8, 1.2 and 1.8 were used giving maximum velocities of 131, 196 and 294 mms^{-1} respectively. The time period, T, for all tests was 8.46s. The flow was assumed to be symmetric so measurements were only made in one half-cycle. Photographs were taken of one of the central ripples at nine phases, ωt, of oscillation from 0° to 180°. Maximum velocity occurred at 90°.

For the wave and current experiments, the flow parameters were chosen to coincide with LDA measurements already carried out in the same tank by researchers at ISVA. The two methods yield very different kinds of information both of which should be useful to numerical modellers.

A set of results for the wave alone was obtained first, to provide a control for the wave plus current cases and to establish how realistic the oscillatory motion really was. The assumption of horizontal oscillation is only an approximation and there is always some vertical motion. Generally the vertical component can be neglected but it will be useful to have a means of checking that the rippled bed does not increase the effect of this vertical velocity on sediment movement. The wave had time period, T, of 2.5 seconds, crest to trough height, H, of 13 cm and orbital velocity near the bed, U_b, of 280 mms^{-1}. The central ripple of the replacement bed, at 15.5 m from the wave paddle, was photographed at sixteen phase positions of the wave from 0° to 360°. (90° is taken to be when the crest of the wave is above the crest of the test ripple.)

Three different currents were then added to this wave, collinear with the wave, such that the ratios of the current velocity to the amplitude of the wave velocity, (U_c/U_b), were 0.36, 0.5 and 0.82. Pictures were taken at the same phase positions. Lastly PIV measurements were made of each of the three currents alone.

As stated in chapter 2, the equilibrium conditions for a ripple are that $a/\lambda \approx 2/3$. Clearly tests osc2 and osc3 do not fulfil this condition. For practical reasons it was easier to test different flows over the same ripple but it should be noted that this may lead to some anomalies. In particular, as the post-shedding

trajectories of the vortices and the ripple geometry are interdependent, the data concerning the motion of the vortices in osc2 and osc3 should probably be treated with caution.

Chapter 4

Data analysis

4.1 Summary

The initial velocity data output from the PIV analysis is most easily presented in the form of velocity field plots. Instantaneous and mean velocity profiles can also be calculated and used to investigate the bottom boundary layers. The other important features of the flows are the vortices. Vorticity is extracted from the full field velocity data and used to locate and identify the extent of individual vortices. Various aspects of the vortices are then measured to characterize and track them. This chapter describes and defines the methods used to do the above.

4.2 Velocity profiles

Horizontal velocity profiles were acquired by averaging the horizontal velocity component, u, horizontally across one ripple length for each row of data throughout the measured depth. This gives a plot of the variation of $\bar{u}$ with height.

Velocity profiles are a more immediate way of assessing the general shape of the flow than the more detailed vector plots. They can also be used to study the development of boundary layers in all the flows. In the flows with a steady component they are used to calculate friction velocities and physical and apparent roughnesses. The details for these calculations are given in the relevant chapter.

Strictly speaking, the velocity profiles have no meaning below the ripple crests. If the ripples are considered to be a form of bed roughness then it is meaningless to assign a mean velocity below the tops of the roughness elements, within the bed. They are given here partly because the ripples are such large roughness elements that the effect the vortices have on the mean velocity before they are shed can be seen and partly because, as discussed in chapter 6, for the purposes of the boundary layers, the vertical origin is not at the ripple crests but at a lower reference level.

4.3 Vorticity

For a velocity field $\vec{u} = (u, v, w)$, the vorticity, $\vec{\omega}$ is defined (see any standard fluids text book for example Lamb or Tritton [34, 56]) as the curl of the velocity field:

$$\vec{\omega} = \nabla \times \vec{u}. \tag{4.1}$$

Thus for 2D motion in the $x-y$ plane, there is only a component of vorticity in the z direction:

$$\omega_z = \frac{\partial v}{\partial x} - \frac{\partial u}{\partial y} \tag{4.2}$$

Vorticity at each point is calculated from the PIV data using an in-house programme which fits a fourth order polynomial to that point and its four nearest neighbours and then finds the gradient.

4.4 Vortex characteristics

The most obvious phenomenon of the flows is the formation and shedding of vortices so some quantification of their characteristics is appropriate.

The new, growing and previous, shed vortices are identified from the contour plots of vorticity magnitudes for each phase in each sequence. Then some means of determining the extent of the vortex has to be found. An outer boundary

was fixed round the vortex where the vorticity dropped to 10% of the maximum vorticity in that vortex. This level is somewhat arbitrary but seemed to give a good compromise between choosing too high a value and therefore cutting off too much of the vortex and too low a value which would mean including some of the background vorticity.

Characteristics of the vortices can then be calculated and the life of a vortex in a given flow can be followed. A number of factors hamper this slightly. The camera has a finite wind-on time so successive phases can not be photographed in the same cycle. Therefore, in this study, one single vortex is not followed through its life-cycle, rather the vortices are from successive cycles. One would not expect the vortices to be completely identical from cycle to cycle so there will be some variation due to this lack of sequentiality.

There are liable to be areas of high velocity gradient near the bed. As described in chapter 3 the PIV analysis system requires a constant velocity within an interrogation area. Thus in areas with a large velocity gradient, the velocity measurements will be unreliable. When the new vortex is growing in the lee of the ripple there are likely to be missing vectors at the bed if seeding at a sufficient density has not reached right into the troughs. Achieving an even seeding density was especially difficult for the experiments at ISVA as explained in the previous chapter, and as also mentioned previously the laser intensity there was never ideal. If there are some missing data points within a vortex, the calculation of the strength of that vortex will be underpredicted. The negatives from the ISVA experiments had to be checked at ISVA during the course of the experiments to

establish that the correct scan rates, shifting speeds, exposure times, focus and so on were being used. The films were developed on site and were inspected with a microscope and tested by shining a low powered HeNe laser through the negatives to check the Young's fringe patterns. This level of 'analysis' was sufficient to ensure that the negatives were good but full analysis could not be done until they were brought back to Edinburgh. Thus any with a lot of missing data points were not discovered until too late. In a few cases there are too many missing data points for calculations about those vortices to be meaningful. Those velocity maps are still of use for qualitative comparisons and for producing velocity profiles above the crest level. Once the vortex has been ejected and is moving in the flow as a fully formed, free entity, it becomes much easier to identify its extent and it is much less likely to contain missing points.

Having established which data points form the vortex a variety of vortex parameters were calculated to define the vortex at each instant:

- Vortex strength/circulation
- Characteristic radius
- X-Centre
- Y-Centre

Thus the strength, size and position of each vortex could be found. Further explanations and the calculations for each of these parameters is detailed below.

4.4.1 Circulation

Saffman [48] describes the circulation Γ around a closed loop, C, as *"a scalar functional of considerable importance in the description of vortex flows"*. It gives a measure of the strength of a vortex.

$$\Gamma = \oint_C \vec{u}.\, d\vec{l}. \tag{4.3}$$

From Stokes' theorem this is equivalent to the flux of vorticity through the surface, S, bounded by the curve:

$$\Gamma = \oint_C \vec{u}.\, d\vec{l} = \int \vec{\omega}.\, d\vec{S}. \tag{4.4}$$

From eqn. 4.4 the circulation round a closed path is equivalent to the sum of all the vorticities in the region bounded by that path. PIV data can be used to yield values of vorticity at each discrete gridpoint so the circulation of a given vortex is found by summing the vorticity, $\vec{\omega_i}$, at each of N points, i, within the vortex and multiplying by the area of a gridcell, A_i.

$$\Gamma = \sum_{i=1}^{N} \vec{\omega_i}\, \vec{A_i}. \tag{4.5}$$

4.4.2 Centre of vortex

The centre of the vortex can be determined in a number of ways: the geometric centre or the point of maximum vorticity are obvious possibilities. The two are not necessarily identical. The maximum vorticity may be offset from the geometric centre, or there may be more than one 'peak' of vorticity within the

same vortex. Neither approach is more obvious than the other. In an attempt to combine them, a 'centre of vorticity' calculation was carried out to weight the geometric centre toward the points of higher vorticity. This is analogous to the more common centre of mass concept. So the horizontal position of this centre, X-centre, was found by:

$$X\text{-centre} = \frac{\sum_{i=1}^{N} \vec{\omega_i} \vec{A_i} x_i}{\sum_{i=1}^{N} \vec{\omega_i} \vec{A_i}} \tag{4.6}$$

where x_i is the x co-ordinate at point i. The equivalent calculation was also carried out for Y-centre, the vertical position.

4.4.3 Characteristic radius

The last parameter to be defined is some kind of measure of the vortex' physical size. A direct geometric calculation of the radius would be plausible if the vortices were neat circles. Following the same arguments as for locating the centre of the vortex, a characteristic radius, R, is found by an averaged, weighted calculation, as follows:

$$R = \sqrt{\frac{\sum_{i=1}^{N} [\omega_i A_i \{(x_i - X_{cm})^2 + (y_i - Y_{cm})^2\}]}{\sum_{i=1}^{N} \omega_i A_i}}. \tag{4.7}$$

Chapter 5

Oscillatory and wave experiments

5.1 Summary

Results from the wave-only experiments are presented in this chapter. This group consists of the three oscillatory and one pure wave motions, table 3.1. To re-iterate, the oscillatory tests were carried out with the ripples upside down in a towing tank and the wave test was carried out separately in a wave flume with the ripples conventionally placed on the base. The purpose of the PIV measurements was to produce velocity data, presented in the form of velocity field plots, and to then extract further information from the plots. Hence it was deemed unnecessary to include many detailed vector plots. A few examples are given with the corresponding vorticity plots. The velocity data is presented in full in the form of velocity profiles. Quantification of the vortex motions and some comparisons with results from the UWB DVM are given.

5.2 Repeatability

In these experiments to study the evolution of the flow, successive pictures are not taken in the same cycle. There is an enforced delay after each exposure for several reasons: the camera has a finite wind-on time; the shifting system has to reset by moving the camera or mirror back to the starting position; in the towing tank experiments, for each new phase, the rippled bed has to be repositioned so that the central ripple crest will be in the centre of the image. Therefore no two photographs are from the same cycle. This poses a problem: are the cycles sufficiently repeatable that this lack of sequentiality is unimportant? To test the repeatability, a film (12 pictures) was taken at the same phase for each of the three oscillations. The most variation was expected around maximum velocity so the test pictures were taken at a phase of 90°. The four vortex characteristics (circulation, radius, X-centre and Y-centre) were found for each frame. Then a mean and standard deviation was found for each characteristic in each oscillation to establish the variation between cycles.

The percentage variations in circulation and radius were calculated by dividing the standard deviation by the mean. Circulation was found to vary by around 10% for osc1 and osc2 but by nearly 20% for the strongest oscillation, osc3. Vortex radius, on the other hand, appeared to become more repeatable with increased amplitude of oscillation, a. It varied by 25% for osc1 but by only 11% for osc3. As the X- and Y-centres are positions rather than sizes the standard deviations are more relevant than percentage errors. The s.d. for the X-centre, 4.7 mm, 6.5 mm and 8.5 mm for osc1, osc2 and osc3 respectively, are small compared

to the ripple length (λ = 220 mm). Similarly for Y-centre the s.d. varied from 2.1 mm to 5.0 mm. Thus, given the complexity of the flow, the characteristics of the vortices are reasonably repeatable with the possible exception of their radii.

5.3 Velocity field plots and profiles

5.3.1 Oscillatory flows

As we are interested in flow over a fixed rippled bed the pictures from the towing tank are manipulated to transform them from their current state of ripples oscillating, upside down, in initially still water to the required flow past stationary ripples. The pictures have been rotated through 180° so that the ripples are the right way up, ie on the bed, underneath the flow. To then get into the frame of reference where the ripples are stationary, the instantaneous velocity of the trolley at the relevant phase is subtracted from each of the vectors in the data set. The camera velocity has already been subtracted during the analysis. As the ripple crest is the obvious reference point, section 3.5, the x–y plane's origin is fixed there.

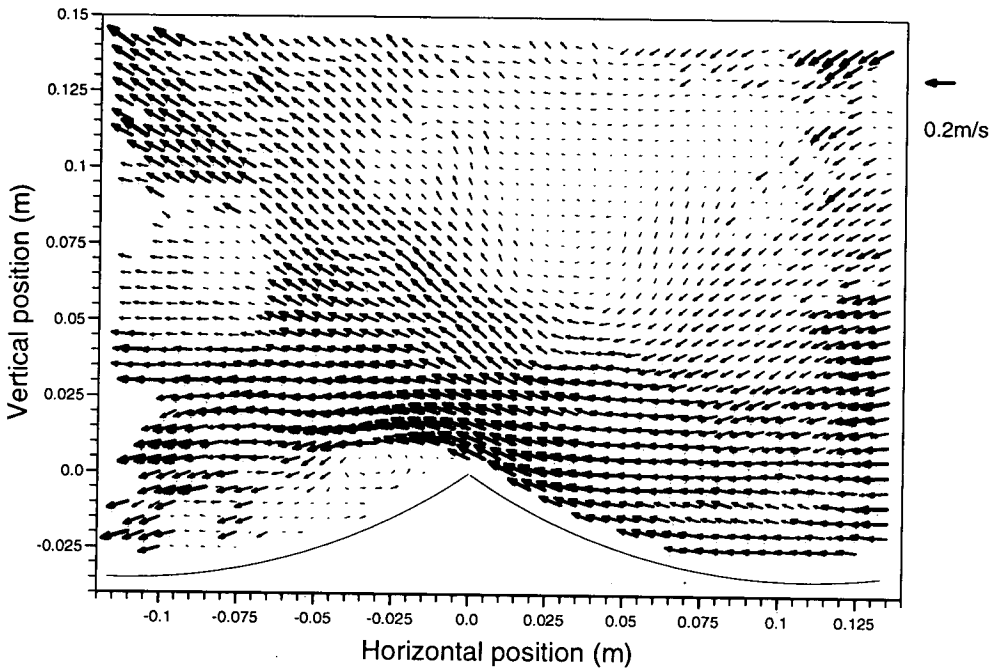

Figure 5.1. Velocity map for osc1, a/L=0.8, ωt=30°.

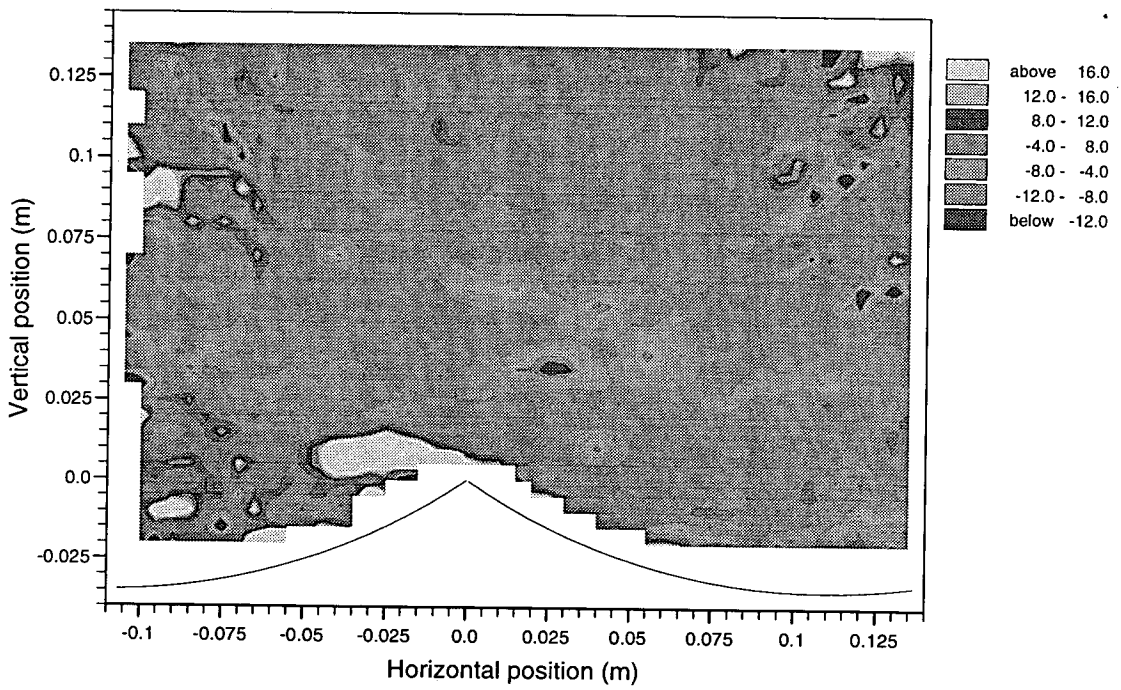

Figure 5.2. Vorticity map for osc1, a/L=0.8 at ωt=30°. Vorticity is in s^{-1}.

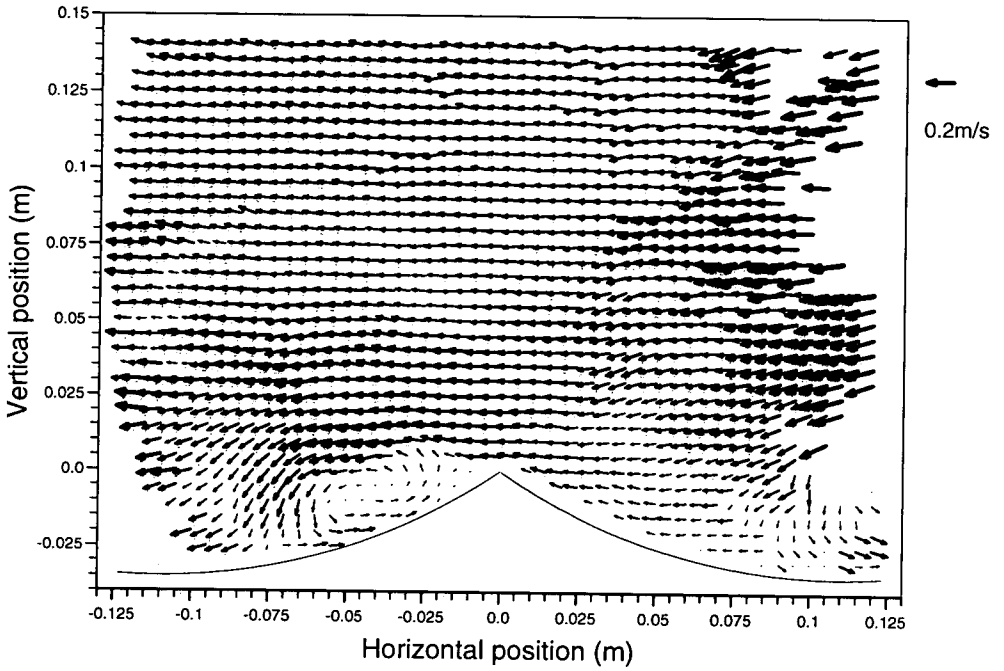

Figure 5.3. Velocity map for osc1, a/L=0.8 at ωt=120°.

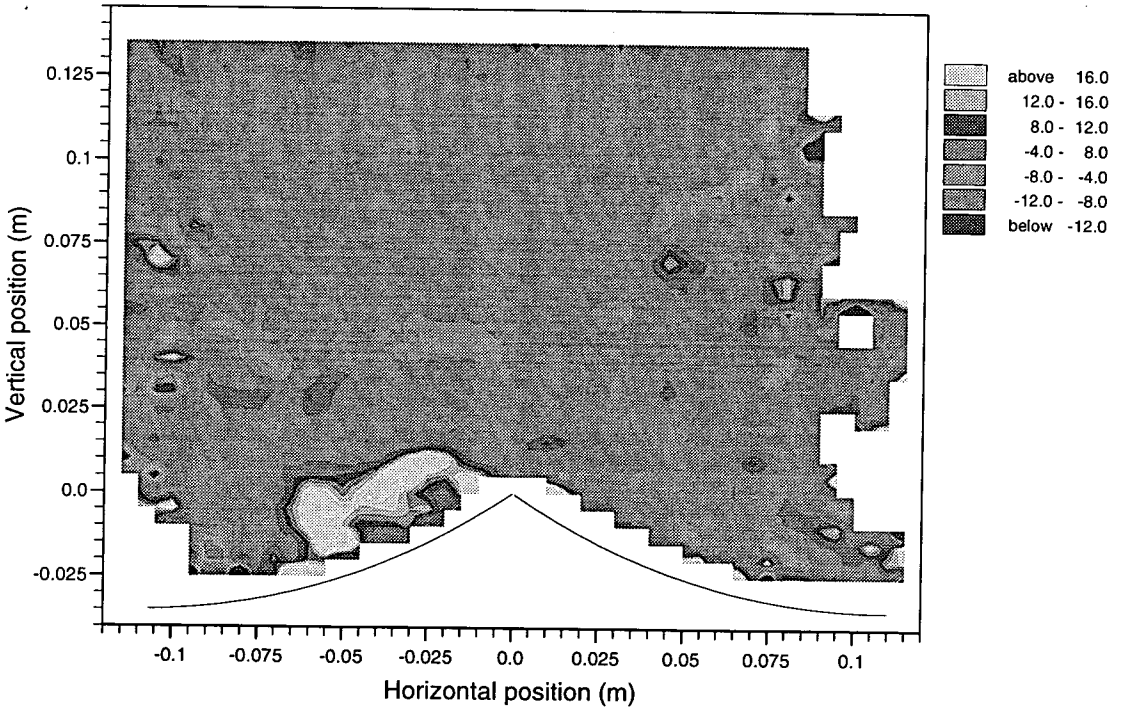

Figure 5.4. Vorticity map for osc1, a/L=0.8 at ωt=120°. Vorticity is in s^{-1}.

Figs. 5.1 and 5.2 are representations of the velocity and vorticity data respectively for osc1, the slowest oscillation. The phase of oscillation, ωt, is 30°, that is the flow has started to accelerate from right to left. A new, positive vortex is growing on the lee side of the ripple and the negative vortex from the previous half-cycle has been ejected into the flow and is moving over the crest. Figs. 5.3 and 5.4 show the same flow later in its cycle. At 120° the flow has passed maximum horizontal velocity and is decelerating. The lee vortex is fully grown but will not be ejected until the flow reverses.

The increased velocities in the upper corners of the velocity map due to the image shifting errors described in chapter 3 and Morrison [42] are noticeable in the top corners of fig. 5.1. As explained previously, although it would have been preferable to have corrected for these errors, they only affect the areas of little interest and as such do not increase the errors in derived results presented later in this chapter.

The horizontal velocity profiles throughout the half-cycles of each of the three oscillations are plotted in fig. 5.5. As expected, the velocities increase towards maxima at a phase of 90° and then decrease again towards flow reversal. The progressive thickness of the growing boundary layers can be measured from the 'turning points' in the velocity profile curves.

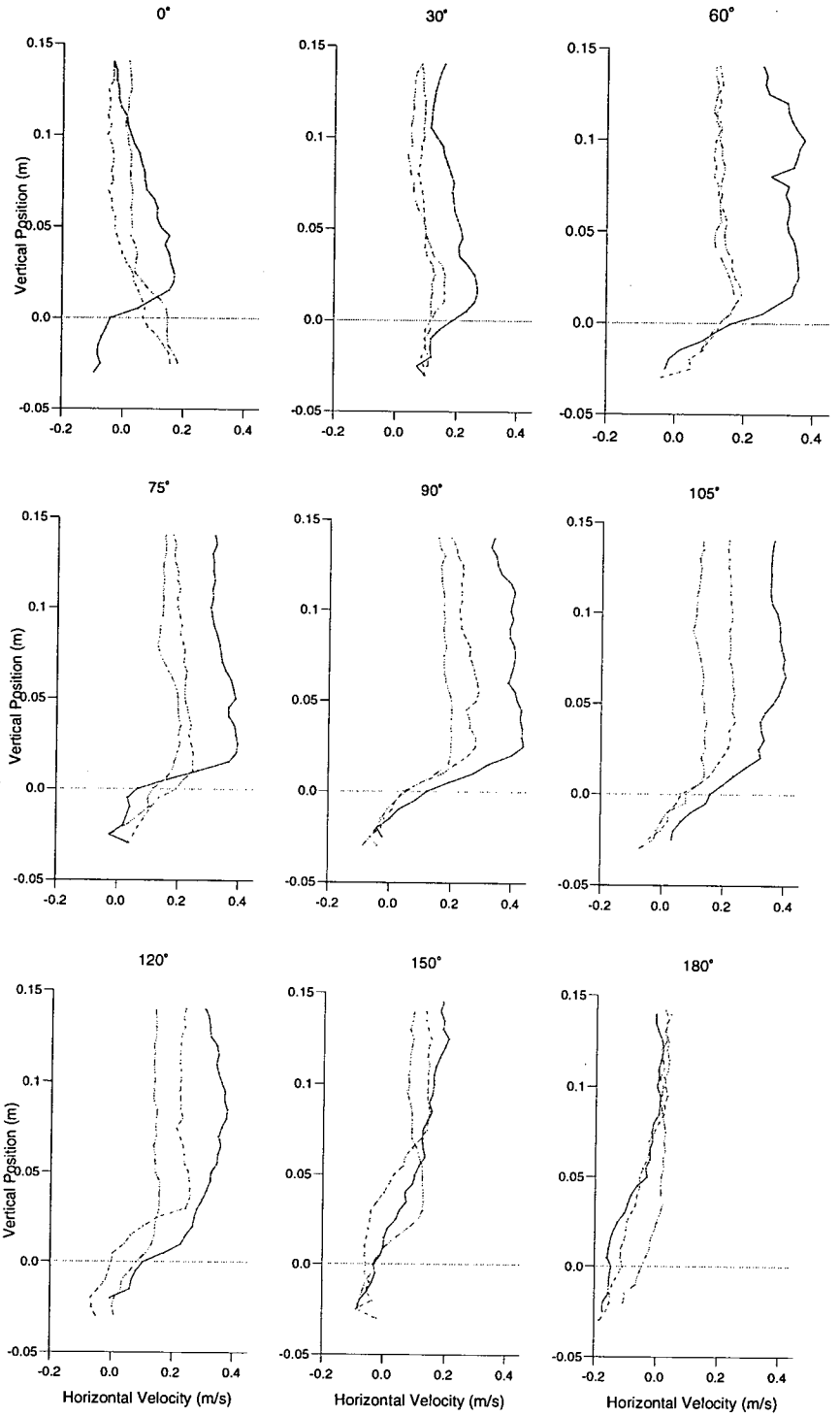

Figure 5.5. Horizontal velocity profiles of the three oscillatory flows throughout the half-cycle. — osc3, - - osc2, — ··· osc1. The maximum velocities of the flows were 294, 196 and 131 mms^{-1} respectively.

Before the boundary layer thickness can be measured, some parameters must be defined. The location of the vertical origin of the $x-y$ plane needs to be more carefully considered if these results are to be compared with other models. Up to now, the vertical origin has been fixed at the ripple crest but there is no reason other than simplicity for assuming this. If the bed is considered rough, the roughness elements being the ripples, then a more logical height for the origin would be somewhere in between ripple trough and crest. It could feasibly be at the average elevation of the roughnesses, or at the level which would be obtained by flattening out all the roughnesses to a smooth surface.

The logarithmic velocity profile in a turbulent boundary layer is discussed in detail in chapter 6. For the purposes of this explanation, it is assumed without further comment that the mean velocity profile for turbulent flow near a rough surface is given [50, 53] as:

$$\bar{u} = \frac{u_*}{\kappa} \log \frac{y-d}{y_0}. \tag{5.1}$$

Here κ is the Von Karman constant, y_0 is a measure of the degree of surface roughness, defined as $y_0 = k_s/30$, k_s is equivalent sand roughness (discussed below) and u_* is the friction, or shear, velocity defined in terms of the shear stress, τ and density, ρ by

$$u_* = \sqrt{\frac{|\tau|}{\rho}}. \tag{5.2}$$

In eqn. 5.1 the vertical co-ordinate, y, has its origin at the base of the roughness elements and d is a displacement height. Jackson [26] tried through an analytical

model and a study of previous literature to determine a physical meaning and an estimate for d. He suggested that d is the height at which the mean drag on the bed appears to act. That is *"...d is determined by the distribution of forces on the* [bed] *surface, whereas the roughness length y_0 is determined by the magnitude of these forces."* He also found that in a wide range of cases $d = 0.7\eta$ was a good estimate, although it would be expected to vary with roughness density or spacing, λ. As the ripples are neither particularly dense nor sparse, this estimate will be used. Thus the effect on the reference level here will be to lower it from the ripple crests by 0.3η. To summarise, when considering the vortex trajectories, the y-origin will be fixed at the ripple crest, to make it easier to visualise the vortex position, but when finding boundary layer thickness the y-origin will be 0.3η below the ripple crests to enable cross-comparison with other models.

In order to determine laws governing the behaviour of flow around rough beds, some means of comparing different types of roughness had to be established. This gave rise to k_s, the Nikuradse roughness length, also known as equivalent sand roughness or physical roughness parameter. The flow moving over and around the individual roughness elements induces spatially varying pressure gradients. This is evident in the case of a rippled bed from the formation of vortices but also happens on a smaller scale around smaller roughness elements. These pressure gradients cause an increase in pressure (or form) drag which is felt by the flow as an increased resistance. The Nikuradse roughness length is a measure of this resistance [50]. For flat beds of sand, k_s is usually related to the diameter of the grains. For rippled beds under waves, Sleath [53] recommends using

$$\frac{k_s}{\eta} = 25\frac{\eta}{\lambda}. \tag{5.3}$$

The constant y_0 in eqn. 5.1 arises as a constant of integration when finding the velocity distribution in a turbulent flow. It is determined from the condition that the turbulent velocity distribution must join the laminar sub-layer close to the bed. For a smooth bed, y_0 is of the order of the thickness of the laminar sub-layer. For a rough bed it is reasonable to assume it is dependent on the roughness parameter and it is found that $y_0 = k_s/30$ [50].

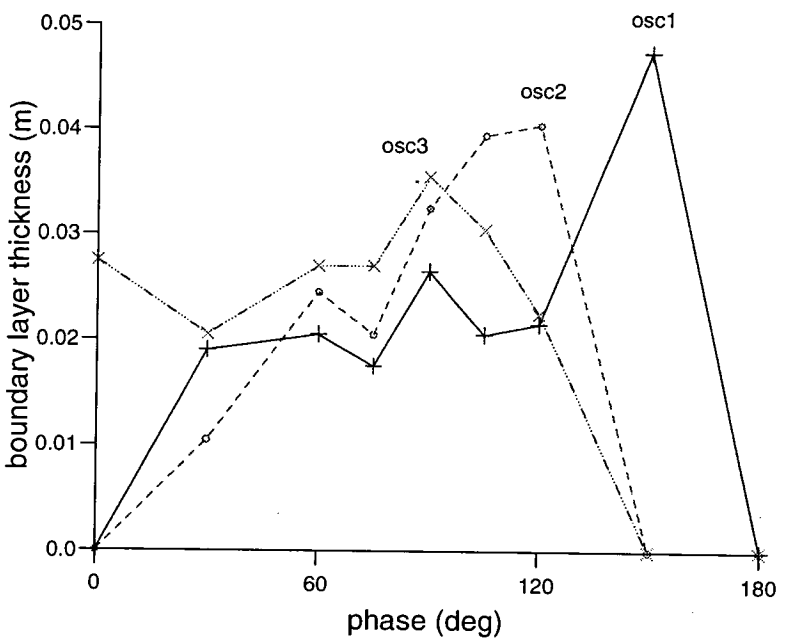

Figure 5.6. Evolution of the boundary layer thickness of the oscillatory flows.

The variation of boundary layer thickness with phase is given in fig. 5.6. The boundary layer for osc3 appears to have developed before the beginning of the half-cycle: the data point at 0° is not zero. The analysis of the relevant negative

was carefully checked and appeared to be accurate. There may have been some error during the experiment or it may be a real effect. It is possibly a result of the flow conditions not fitting in with the equilibrium conditions for the ripple as discussed in section 3.6.

Fredsøe [15] suggests a model for calculating the thickness, δ_w, of an oscillatory boundary layer over a rough bed. It uses similar arguments to those developed by Jonsson and Carlsen [30] whereby the velocity profile is assumed to be logarithmic in the boundary layer and then the equation of momentum is applied in that layer. The case where the water outside the boundary layer moves with velocity

$$u = U_0 \sin \omega t,$$

where U_0 is the maximum velocity outside the boundary layer, is studied. The flow is only considered for one half-cycle, thus the effect of vortices formed by previous motion is ignored. The model is intended for use over a rough bed where the time period of the oscillation is much larger than the life-time of the eddies created between roughness elements. This is evidently not the case for a rippled bed but in the absence of a convenient alternative, Fredsøe's results will serve as an indication of expected boundary layer thickness.

In the model, the boundary layer is shown to grow throughout the half-cycle and values are given for predicted δ_w for a given amplitude of oscillation, a, and bed roughness, k_s. Jonsson suggests measuring δ_w as the thickness of the boundary layer at 90°, the point of maximum velocity in the outer flow.

	a/k_s	δ_w (cm)	$\delta_w(1)$ (cm)	$\delta_w(10)$ (cm)
osc1	1.3	2.65	3.2	1.3
osc2	1.9	3.25	4.8	1.95
osc3	2.8	3.55	7.2	2.9

Table 5.1. Comparison of measured and Fredsøe's predicted values for boundary layer thickness, δ_w. Values for $\delta_w(1)$ are predictions for flows with $a/k_s = 1$, those for $\delta_w(10)$ for $a/k_s = 10$

Fredsøe quotes values of δ_w/a for $a/k_s = 10^0, 10^1, 10^2 \ldots$ Experimental values of a/k_s vary from 1.3 to 2.8 so in table 5.1 the measured values of δ_w are compared to predictions for $a/k_s = 1$ and 10. The measured values for all the oscillations lie between the limits given by the two predicted values. In fig. 5.6 the boundary layers stop growing earlier in the half-cycle for increasing amplitude of oscillation, contrary to the model where δ_w continues to increase until flow reversal. Thus the model may not predict the full development of boundary layers to the end of the half-cycle, but does give a reasonable indication of expected boundary layer thickness at maximum free stream velocity.

5.3.2 Pure wave

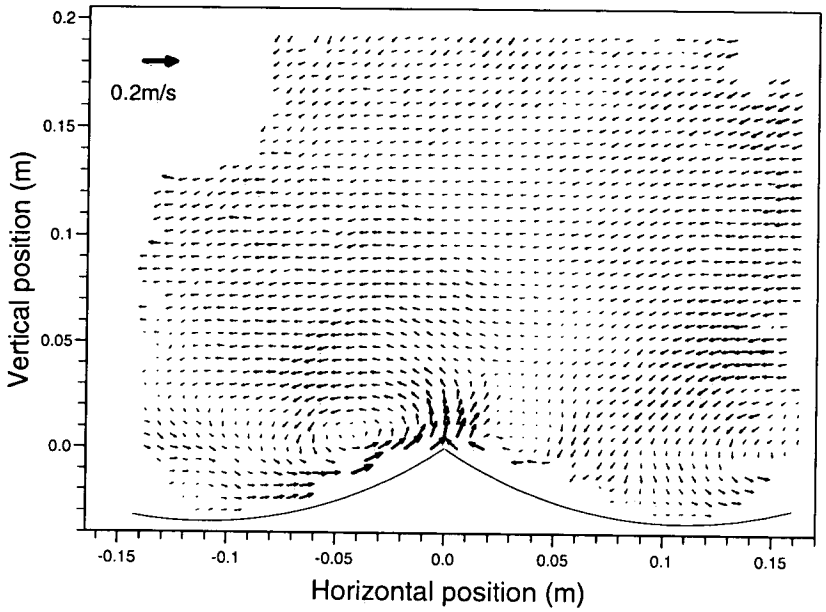

Figure 5.7. Velocity map of average flow under the wave.

Fig. 5.7 is the velocity field plot of the average flow under the wave over one wave period. The measurement zone was 0.2 m deep, half the water depth, which was 0.4 m. Measurements were made throughout the whole wave-cycle because, unlike for the purely oscillatory cases, the two half-cycles could not be assumed to be identical. The average was obtained by adding the velocity fields from each phase in the wave cycle together, weighting each phase contribution by an appropriate fraction of the time period, T. The wave is travelling from left to right however the mean motion in fig. 5.7 is right to left, against the direction of wave propagation. This is further illustrated in the space and time averaged velocity profile, fig. 5.8. Near the bed, the velocity is positive. It reverses about 7 mm above the ripple crest level. Longuet-Higgins [37, 38] describes how the

forwards drift in the boundary layer arises. In a progressive wave, forward velocities are found near both the bottom and the free surface, with a negative velocity in between. As this work was concerned with flow patterns near the bed, no measurements were made near the surface so the expected flow reversal at the surface cannot be observed.

The other features of fig. 5.7 are the two recirculating cells, one on either side of the ripple crest. The positive one, on the left hand side, is considerably larger than the negative, right hand side, one. Possible reasons for this will be discussed in section 5.4.1.

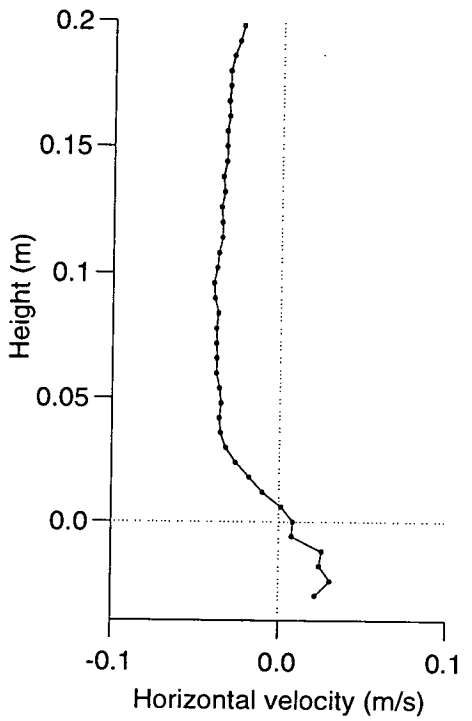

Figure 5.8. Mean velocity profile of the pure wave flow.

5.4 Life-cycles of the vortices

The calculated vortex characteristics are now presented. As already stated, measurements were only made for one half-cycle of the oscillatory flows. In this section, both the new growing vortex and the shed vortex from the previous half-cycle were tracked from picture to picture throughout the half-cycle. To make it easier to follow the life-cycle of a vortex, the characteristics of the new vortex are plotted as calculated but the horizontal positions of the shed vortex have been reflected about the crest and the strengths multiplied by -1. Thus the characteristics are presented as continuous data of the life-cycle of one vortex.

In the pure wave case, measurements were made throughout the cycle and therefore two sets of vortex characteristics were obtained. One from a negative vortex ($\omega-$) under the wave crest and one from a positive vortex ($\omega+$) under the trough. These two vortices would not be expected to be identical. To make it easier to compare the two vortices, the negative vortex circulation has been multiplied by -1 and the positive vortex, which begins its cycle 180° into the wave cycle, has been shifted back 180° in these graphs.

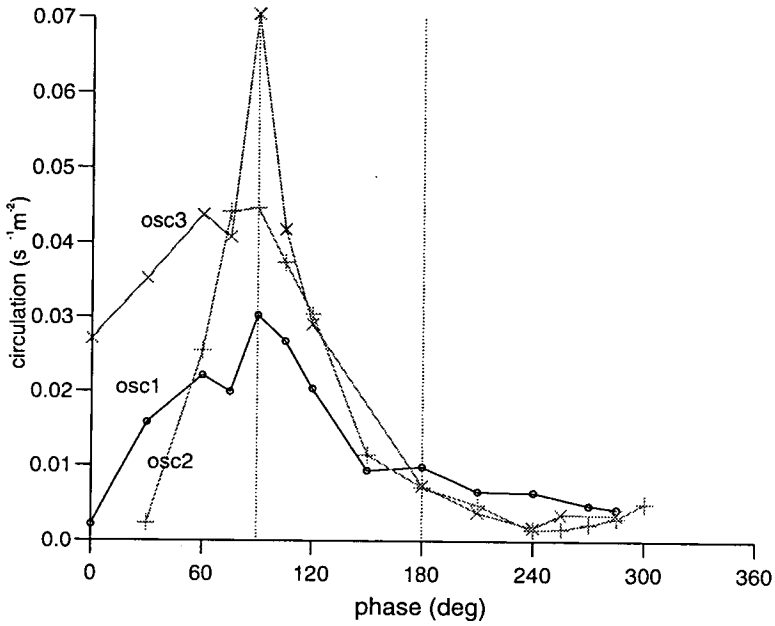

Figure 5.9. Variation of vortex circulation with phase for each of the three amplitudes of oscillation. Symbols as follows: • - osc1, + - osc2 and x - osc3.

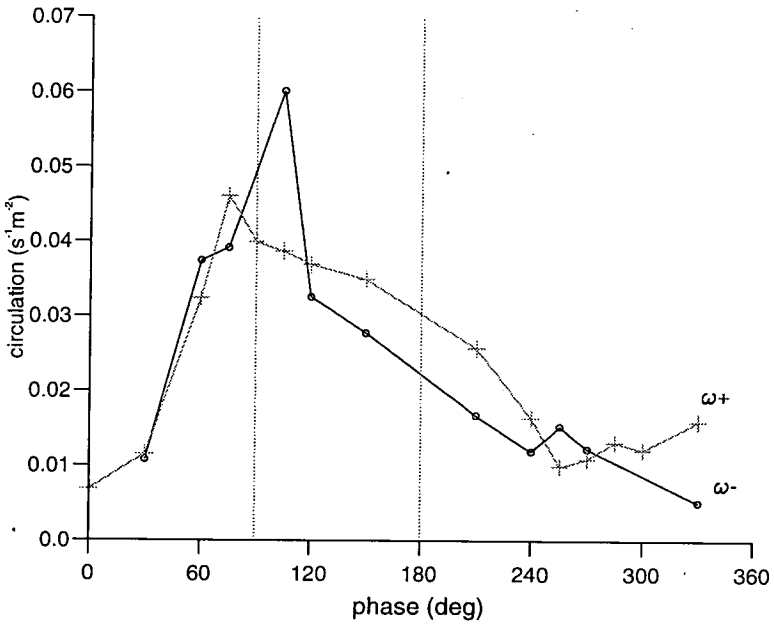

Figure 5.10. Vortex circulation of the two vortices in the wave cycle. The negative vortex, $\omega-$, is given by • and the positive one, $\omega+$, by +.

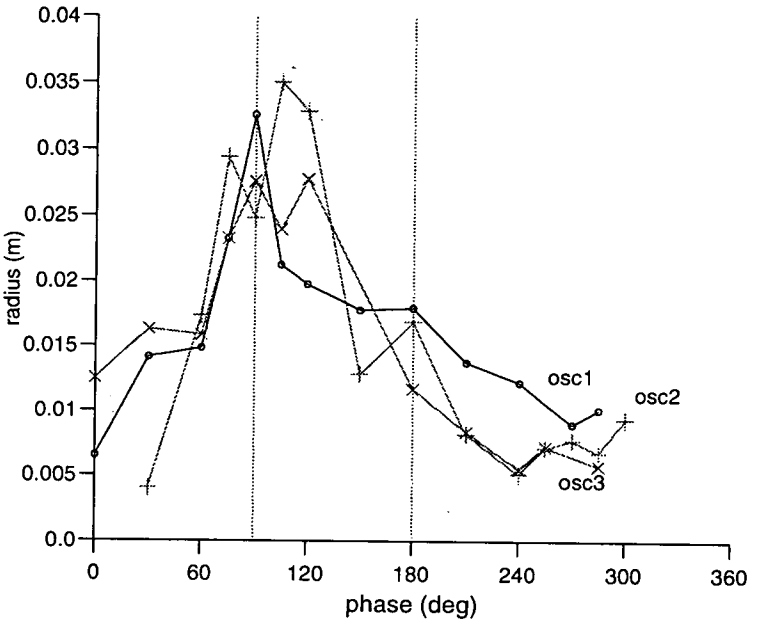

Figure 5.11. Radii of vortices in oscillatory flows. Symbols as before: • - osc1, + - osc2 and x - osc3.

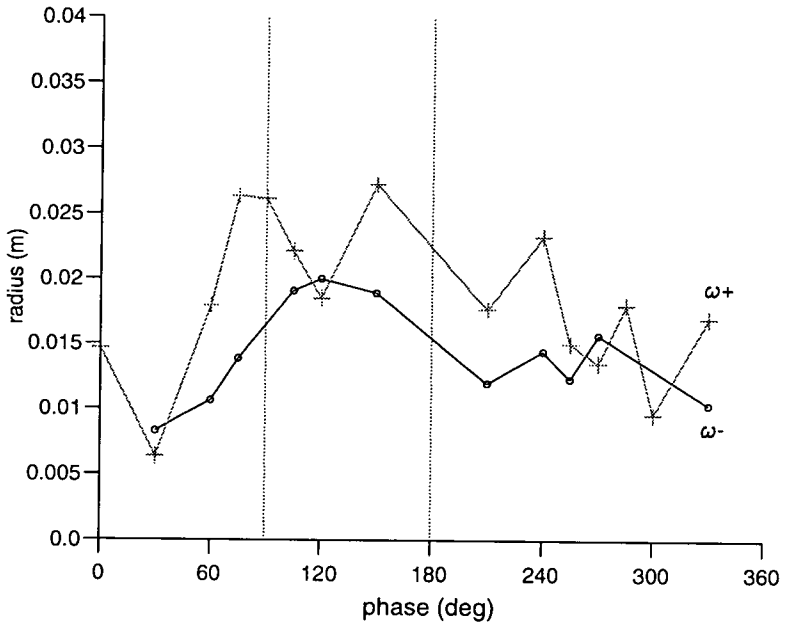

Figure 5.12. Radii of vortices under the wave. Symbols as before: $\omega-$ - •, $\omega+$ - +.

5.4.1 Vortex circulation and radius

The variation of vortex strength with phase for each of the oscillations is plotted in fig. 5.9. The vortices all start to grow at the beginning of the half-cycle, reaching maximum strength at 90°, the largest oscillation producing the largest circulation. As the flow begins to decelerate, the vortices begin to dissipate. The dimensions of the vortices do not appear to depend strongly on amplitude of oscillation according to fig. 5.11. They all grow to a maximum radius of around 35 mm, or approximately one ripple height, η. Maximum size is reached rapidly at or just after 90°, at the same time as maximum circulation.

Tunstall and Inman [57] found vortex diameter to be independent of wave conditions, near the equilibrium conditions for that ripple. They also found maximum vortex diameters to vary between η and 1.4η. This would give expected radii for this ripple height of 17.5 - 24.5 mm — smaller than measured here. However, their experiments were over natural, round-crested ripples. Horikawa and Mizutani [25] found that vortices shed from sharp crests were considerably larger than those from round crests in accordance with the results presented. It also appeared that for sharp crests, flow separation occurs at the beginning of each half-cycle, as seen here. For Tunstall and Inman's round crested equilibrium ripples separation occurs later at $\omega t = 90°$, the point of maximum horizontal velocity.

The vortices under the waves reach a similar circulation to those under oscillatory flow, as shown in fig. 5.10. The negative vortex, $\omega-$, is stronger than

the positive one, $\omega+$, before it is shed but it dies away faster. There are two mechanisms operating here. Shown in fig. 1.2, a negative vortex is formed on the right hand side of the ripple under the wave crest (if the wave is travelling from left to right). After flow reversal, a positive vortex is formed on the other side. If the flow is symmetric these two vortices would be expected also to be symmetric. However, when Stokes' linear wave theory is extended to second order, the wave loses its symmetry [11]. The horizontal velocities are increased under the crest and decreased under the trough [38, 11] leading to a dissymmetry between the two lee vortices during formation. The negative vortex, $\omega-$, produced under the wave crest will be stronger than $\omega+$, formed under the wave trough. This effect is counteracted by the presence of a velocity gradient in the mean flow. If the mean horizontal velocity, $\bar{u}$, is broken down into contributions from the wave motion, $\bar{u}_w$, and the vortex, $\bar{u}_v$, so that:

$$\bar{u} = \bar{u}_w + \bar{u}_v$$

then mean vorticity, from eqn. 4.2 is

$$\bar{\omega}_{tot} = \frac{\partial \bar{v}}{\partial x} - \frac{\partial}{\partial y}(\bar{u}_w + \bar{u}_v).$$

The vorticity due to the vortex is then given in this notation by

$$\bar{\omega} = \frac{\partial \bar{v}}{\partial x} - \frac{\partial \bar{u}_v}{\partial y}$$

so an additional vorticity is given by

$$\delta\bar{\omega} = -\frac{\partial \bar{u}_w}{\partial y}. \tag{5.4}$$

In the case of a purely sinusoidal flow $\frac{\partial \bar{u}_w}{\partial y} = 0$ and the only contribution to the vorticity is by the vortex. However, for a wave, from fig. 5.8, the mean flow close to but not right at the bed has a negative velocity gradient and therefore a positive vorticity. This bulk positive vorticity acts to reinforce the positive vortex and reduce the negative one [58]. Thus the negative vortex is initially stronger due to Stokes second order non-linearities in the wave but decays faster than the positive vortex as the bulk vorticity acts against it.

The vortices under the wave are smaller than those due to oscillatory flow, the maximum radii being 2 cm for $\omega-$ and 2.8 cm for $\omega+$, fig. 5.12. The data seem to indicate that the vortices in all cases have a life expectancy of about one time period before they break down.

5.4.2 Vortex trajectories

The horizontal position calculations are the smoothest. In the oscillatory bed case, fig. 5.13, the X-centre moves towards the trough as the vortex grows. There is very little difference between the three data sets while the vortices are still growing. The trajectories separate when the flow reverses and the vortices are ejected. At 285°, towards the end of the cycle, the vortex in osc1, the slowest motion, has moved to about 0.2 m, that is approximately one ripple length away from the 'parent' crest. In the fastest flow, osc3, the vortex has been carried about 0.45 m,

about 2 ripple lengths.

The vertical positions, plotted in fig. 5.15, are less well defined. The vortices, as expected, stay near the bed until they are shed. As they grow and move horizontally away from the crests, they also move down further into the troughs. When they are shed they are lifted up to around 5 cm, about 1.5η. From the data there does not seem to be much difference in height reached between the oscillations, which is probably to be expected in purely horizontal motions.

The X-centre of the vortices under the pure wave, fig. 5.14, again moves slightly towards the trough as the vortices grow. At about 120° they are carried towards and then over the crest. In accordance with the above argument for second order non-linearities in the wave, the trajectories for the positive and negative vortices are not symmetric. Comparing the displacements at 330°, $\omega-$ has travelled 12 cm whereas $\omega+$, transported by the stronger wave crest induced motion, has travelled about 18 cm.

Fig. 5.16 shows more clearly that, as suggested for the oscillatory flows, when the vortices move horizontally away from the crests they also move down into the troughs slightly, by about 1 cm. At about 120° they are carried up and over the crests to about 4.5 cm, comparable to the height reached in the oscillatory flows.

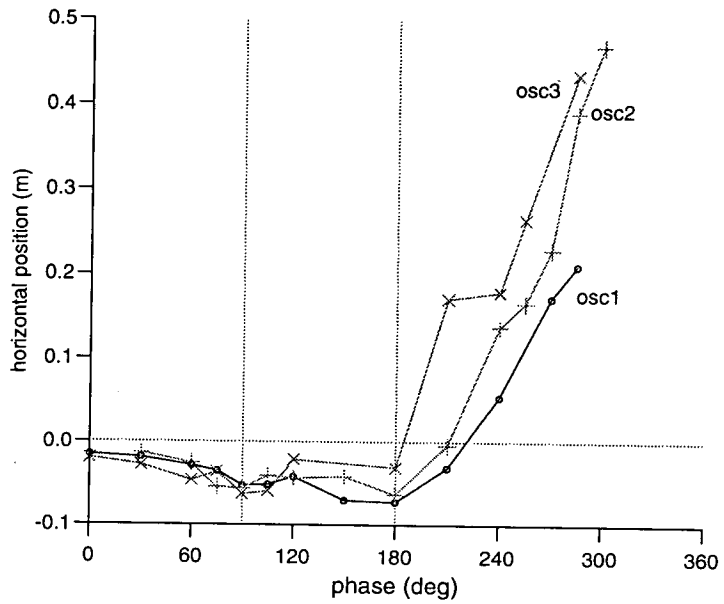

Figure 5.13. X-centre of vortices in oscillatory flows. Symbols as before: • - osc1, + - osc2 and x - osc3.

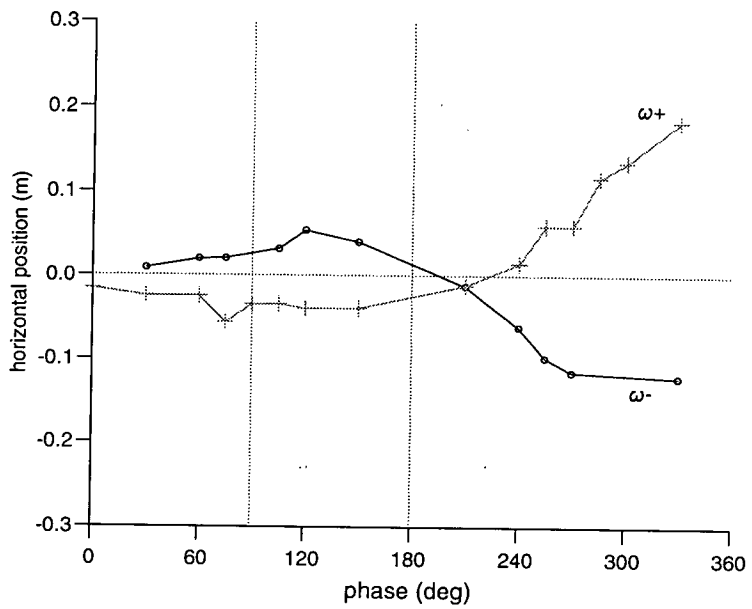

Figure 5.14. X-centre of vortices under the wave. Symbols as before: $\omega-$ - •, $\omega+$ - +.

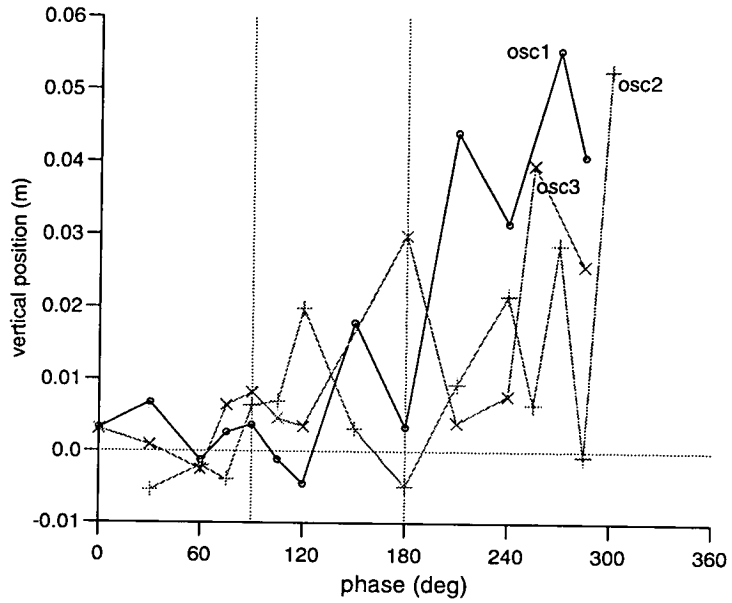

Figure 5.15. Y-centre of vortices in oscillatory flows. Symbols as before: • - osc1, + - osc2 and x - osc3.

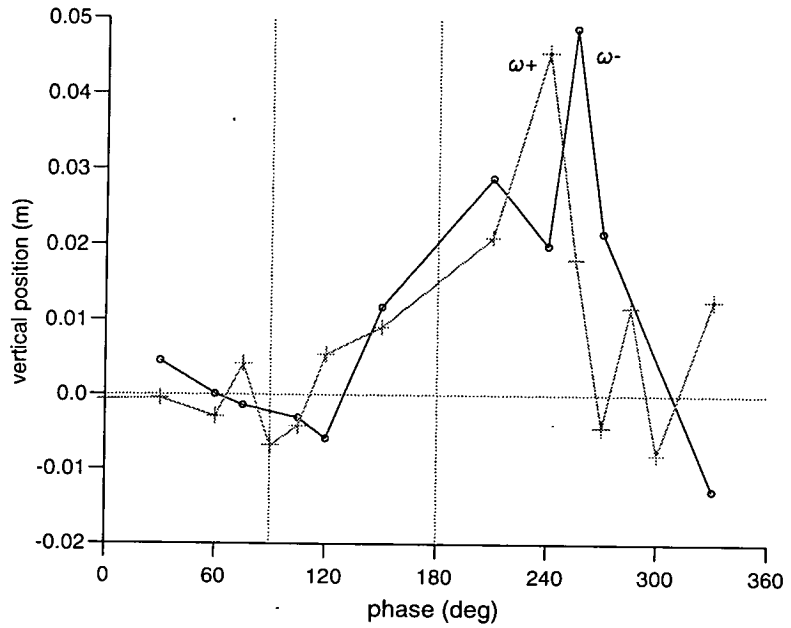

Figure 5.16. Y-Centre of vortices under the wave. Symbols as before: $\omega-$ - •, $\omega+$ - +.

5.5 Comparisons with discrete vortex model

In this final section of this chapter, the measured vortex characteristics are compared to the predictions of the round crested, discrete vortex model (DVM) developed at the University of Wales (UWB). A full description of the model is given by Block [4] and a comparison with some experimental measurements of sediment concentration over a bed of sand ripples in oscillatory flow by Block et al [5]. The model is an extension of the type proposed by Longuet-Higgins [39] which makes use of a conformal mapping of the irrotational flow to facilitate calculations of the flow over the ripples. Every time-step a point vortex is introduced into the flow at the ripple crest. These vortices are then advected and amalgamated in subsequent time-steps, causing a large vortex (with a rotational core) to grow on the lee side of the ripple every half-cycle.

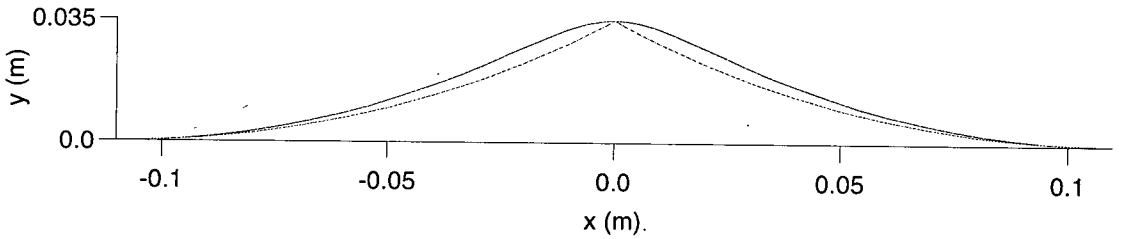

Figure 5.17. The experiment's sharp crested ripple shape (dashed line) and the model's round crested ripple (solid line).

Although the two crest shapes are clearly different as shown in fig. 5.17, the simple method of forcing vorticity to enter the flow at the crest in the model should imply that the locations of the vortices more closely mimic those in the experiment over sharp crests. On the other hand, because of the need to keep

the DVM irrotational, the vorticity is kept too localised around the vortex core to give an accurate prediction of the radius of the vortex. The free stream velocity is purely horizontal in the model which makes it ideal to compare with the oscillatory flow experiments. For this ripple steepness, $\eta/\lambda = 0.16$, the model is valid in the range $0.5 < a/\lambda < 1.6$ so osc1 and osc2 are used, osc3 being outwith this range.

The four calculated characteristics of the vortices in the two cases are plotted with the corresponding model predictions in figs. 5.18, 5.19, 5.20 and 5.21. The model predicts the growth and decay of vortex strength reasonably well but with a time-lag. This lag is understandable given that vortex formation would be expected to occur earlier for the sharp crested ripples than for the round ones [25]. In fig. 5.9 it looked as though the experimental measurement of circulation for osc2 was too low around phase $\omega t = 90°$. This would then imply, fig. 5.18, that the model slightly underpredicts maximum circulation in both cases. This can again be attributed to the difference in the ripple profiles — Horikawa and Mizutani [25] also found that the vorticity of the vortex from a sharp crested ripple is stronger than that from an otherwise similar round crested one. The vortex radius curves differ, fig. 5.19, as expected; the vorticity in the model being constrained to lie too close to the axis of the vortex. The predictions of horizontal motion of the vortices, fig. 5.20, for both oscillations are consistent with the experimental data. The plots of vertical motion appear to agree less well. The height might be expected to be underpredicted due to the absence of vertical diffusion in the model. This disparity is emphasised by the scale as the vertical axis only covers a few centimetres or about 2η. The Y-centre is plotted against

phase in fig. 5.21. However, the flow near the ripples would be expected to follow the shape of the ripples to some extent and therefore the height of a vortex at a given instant will depend on its horizontal position. When the trajectories of the vortices, rather than absolute height, are plotted, as in fig. 5.22, the comparison is much better, especially for osc2.

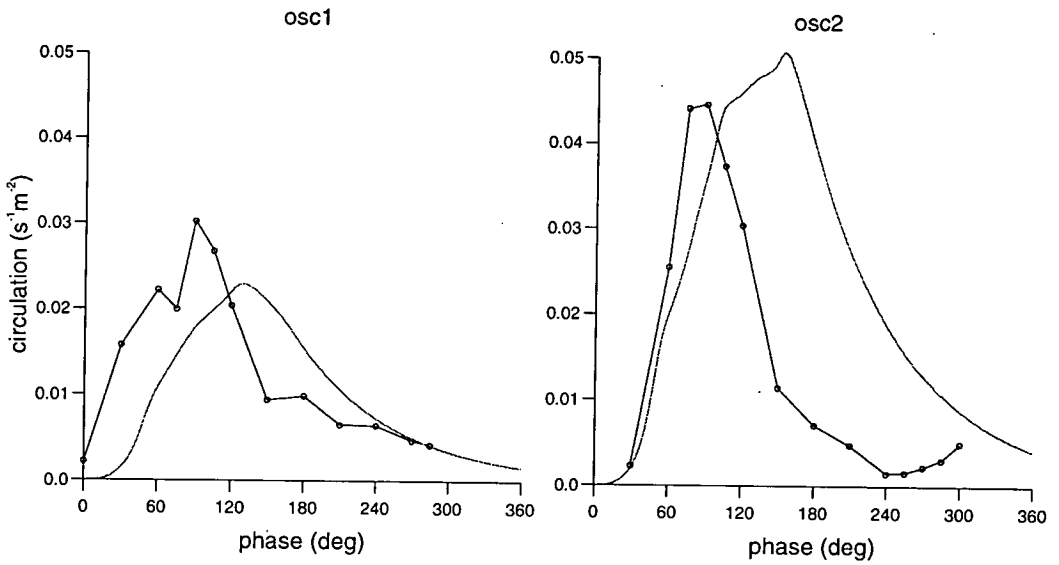

Figure 5.18. Comparison of circulation of vortices in osc1 and osc2 with DVM predictions. Symbols: • - experiment and solid line - model.

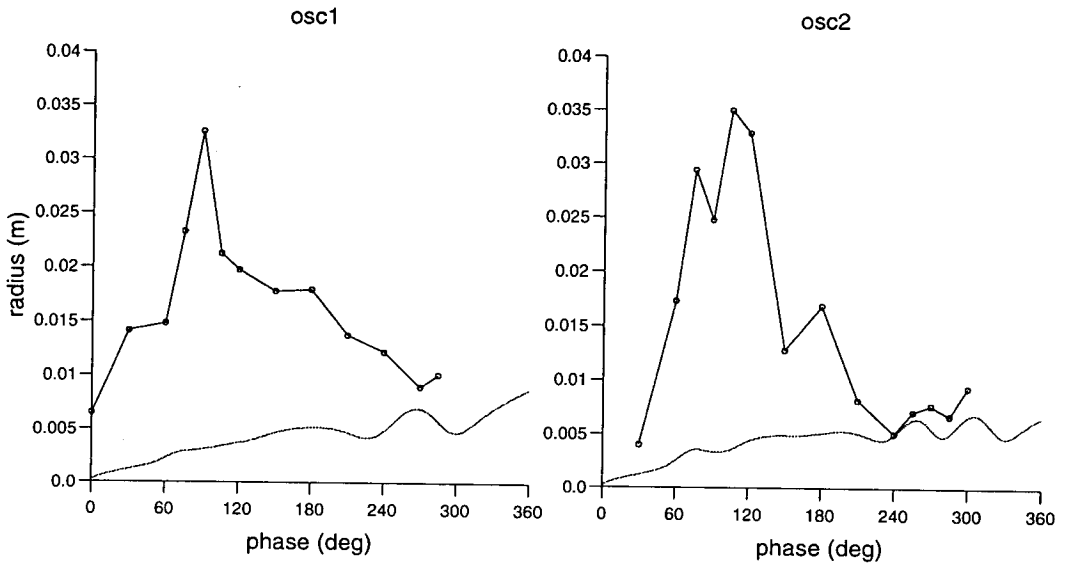

Figure 5.19. Vortex radius. Symbols: • - experiment and solid line - model.

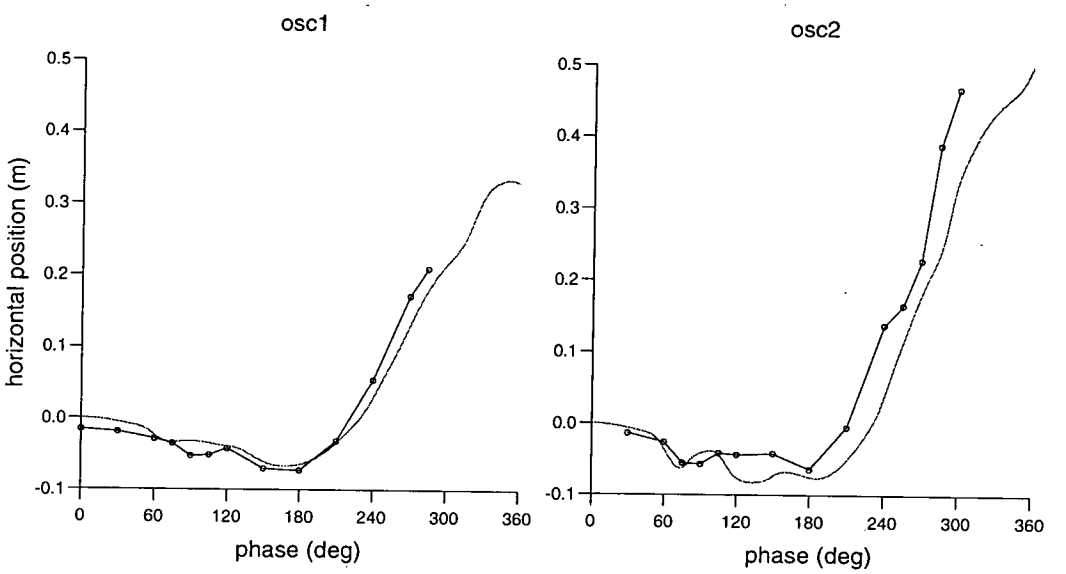

Figure 5.20. X-centre of vortex. Symbols: • - experiment and solid line - model.

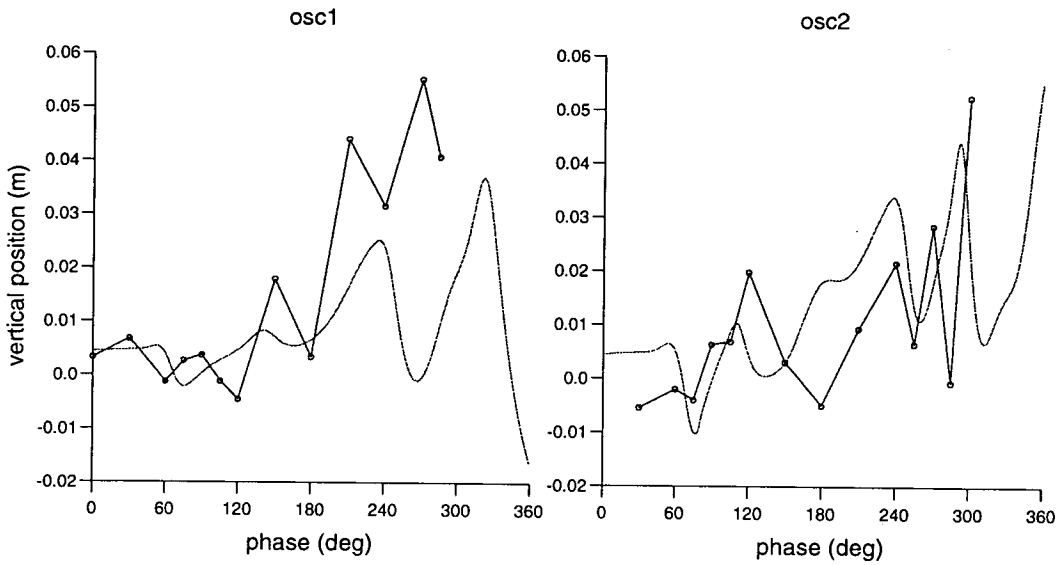

Figure 5.21. Y-centre of vortex. Symbols: • - experiment and solid line - model.

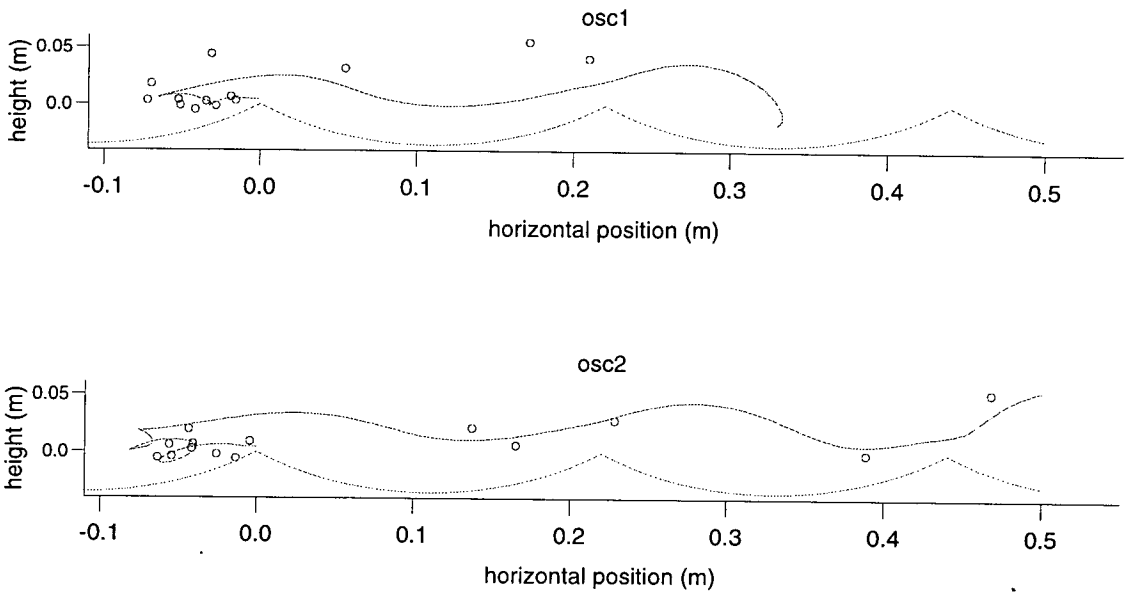

Figure 5.22. Trajectories of vortices over the ripple bed. Experimental measurements given by o, model prediction by solid line.

Having established that the UWB discrete vortex model was able to predict the strengths and trajectories of the vortices reasonably well under oscillatory flow, it was then tested against the wave data.

The model is driven by the free stream velocity at the edge of the boundary layer so the first step was to determine this velocity from the experimental data. Malarkey [40] used the horizontally averaged horizontal velocity from the top of the measurement zone for each phase throughout the cycle to provide a time series of free stream velocity. This time series was then fitted to a mean, first and second harmonic as shown in fig. 5.23. However, the model produces its own mean velocity, generated by the vortices, which tends to zero a long way from the bed, so only the first and second harmonics were used in the model free stream. Ideally, a process whereby the horizontally averaged mean velocities were matched between the model and data at particular heights to determine an optimum height for the free stream velocity would be carried out. However, changing the mean by reasonable amounts was found to have little effect on the results so the approximation described was used.

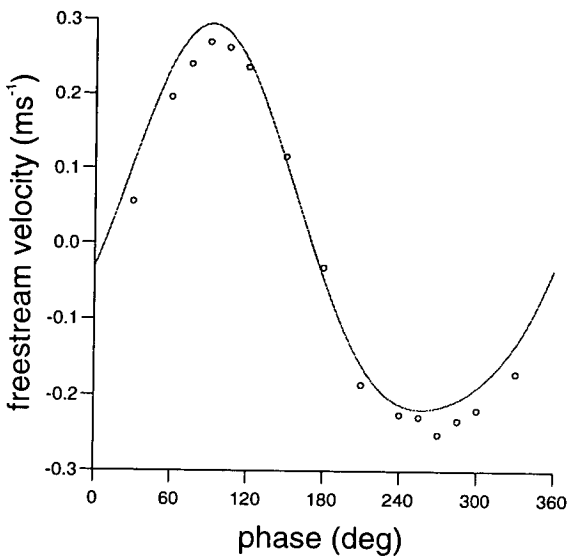

Figure 5.23. Free stream velocity at the edge of the boundary layer. Experimental measurements given by o and the curve fitted to them by the solid line.

The comparisons of the experimental and model results for the positive and negative vortices, $\omega+$ and $\omega-$, are given in figs. 5.24, 5.25, 5.26 and 5.27. The circulation is underpredicted for both vortices which might be due to the different ripple profiles. However, the shapes of the two plots do agree with the experiment. The negative vortex is initially stronger but loses strength rapidly compared to $\omega+$ which has a lower, fatter circulation profile. The radii data are not included because it has already been demonstrated that this model underpredicts the spread of vorticity. The X-centres, fig. 5.25, are again predicted well except that $\omega-$ is advected too far in the model. The Y-centres are again not lifted high enough. The vortex trajectories, fig. 5.27, show this more clearly, demonstrating that additional vertical diffusion is needed in the model.

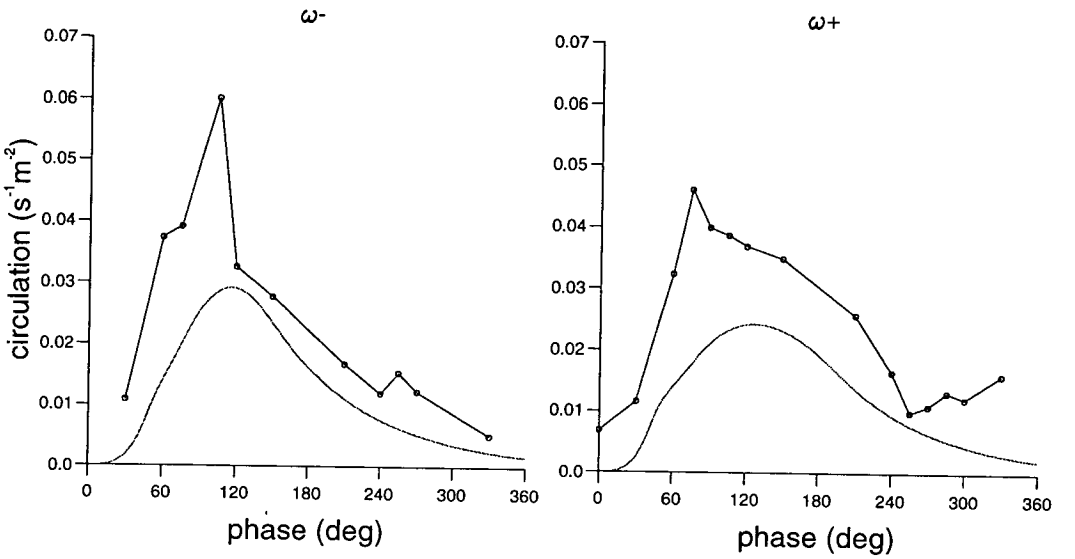

Figure 5.24. Comparison of circulation of vortices $\omega-$ and $\omega+$ under the wave with DVM predictions. Symbols: • - experiment and solid line - model.

In general this section has shown the approach of the discrete vortex model to be successful in predicting the life-cycles of the vortices under both sinusoidal motion and a wave. On the basis of these comparisons, the first improvement to the model would be to introduce some form of vertical diffusion.

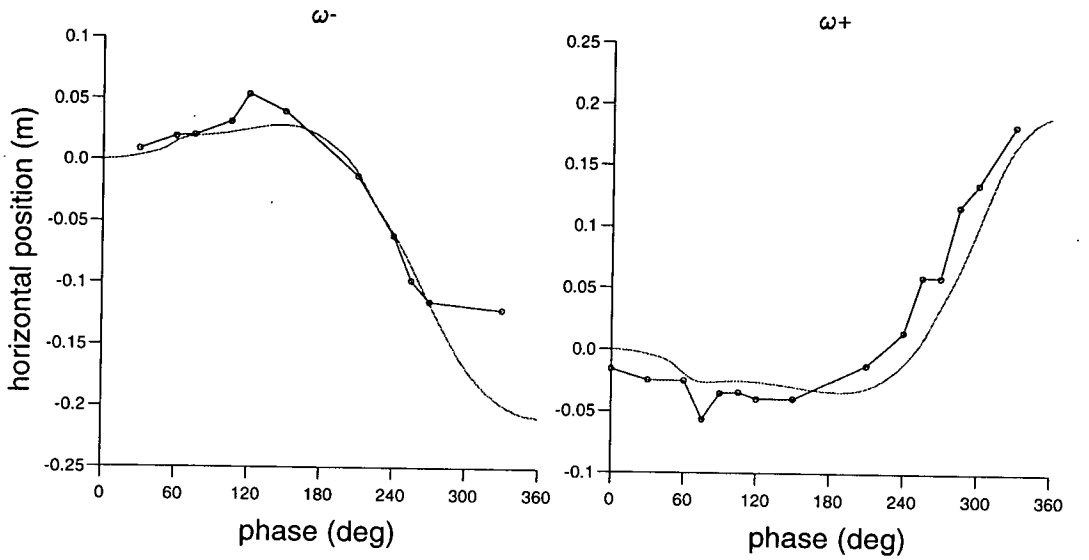

Figure 5.25. X-centre of vortex. Symbols: • - experiment and solid line - model.

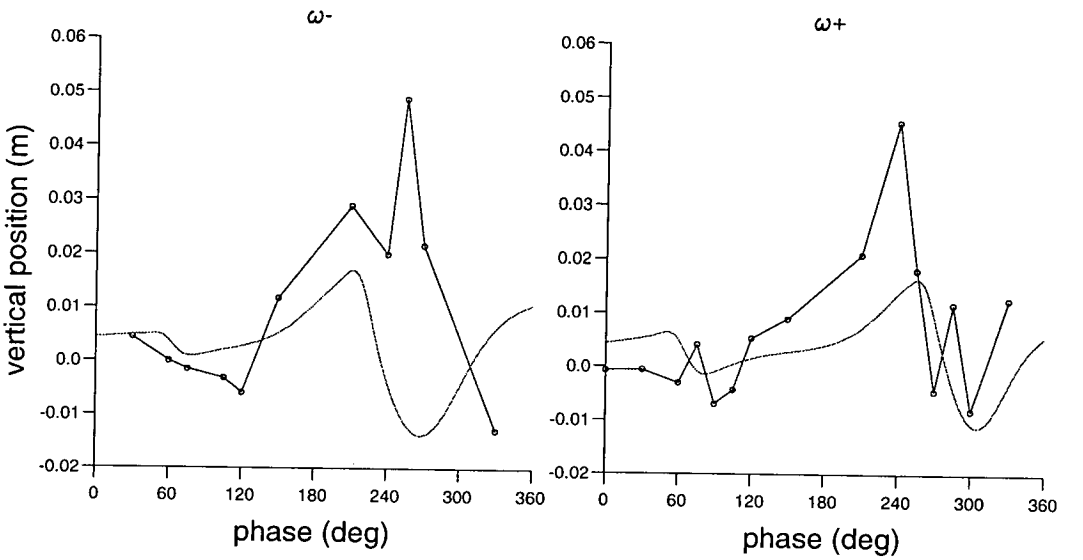

Figure 5.26. Y-centre of vortex. Symbols: • - experiment and solid line - model.

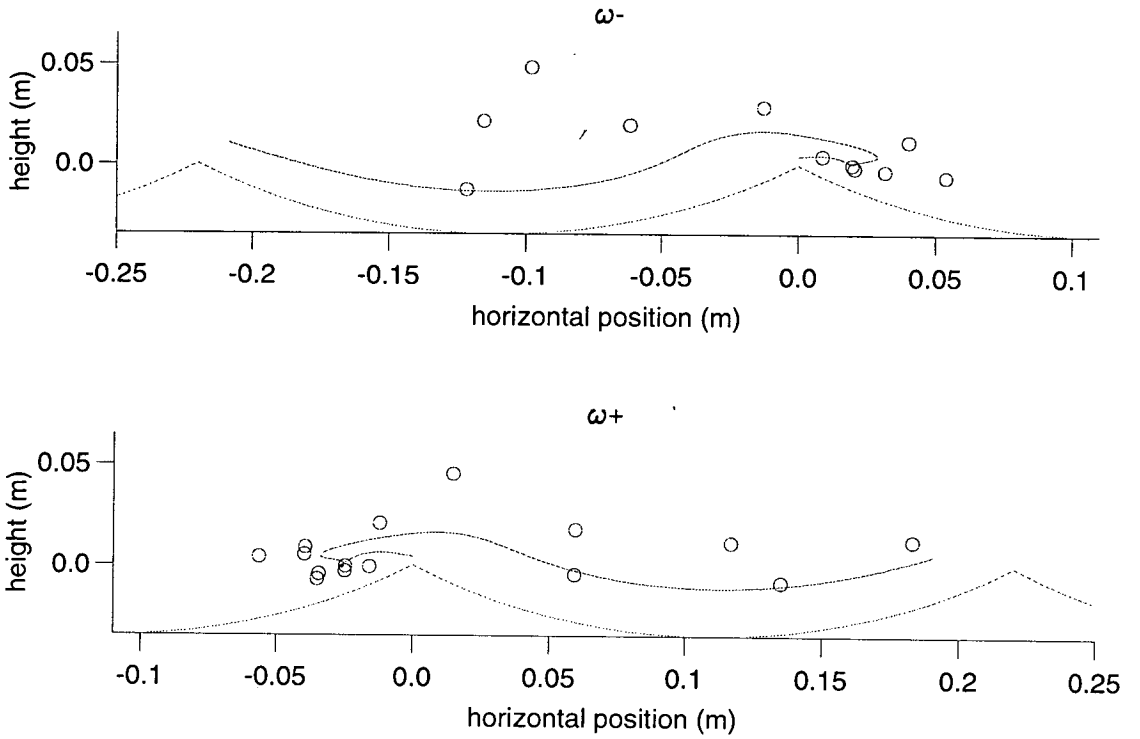

Figure 5.27. Trajectories of vortices over the ripple bed. Experimental measurements given by o, model prediction by solid line.

5.6 Concluding Remarks

High quality PIV measurements of oscillatory and wave flows over ripples were obtained and used to investigate properties of the two main features of the flows: the boundary layers and the vortices.

Data from the oscillatory boundary layer calculations were compared to a simple model with, given the simplicity of the model, good agreement. The velocity profile of the cycle-averaged wave flow showed flow reversal close to the bed, giving the bulk of the flow within the measurement depth a mean negative

velocity. This reversal and the asymmetry between the forward and reverse flows under the wave were shown to have an observable effect on the vortices formed during the wave motion.

The calculated vortex characteristics in all cases were seen to be reasonable compared to findings described in the literature. They were then used to assist with validation of the UWB DVM. It was found that the model predicted strengths and trajectories, but not radii, of the vortices well and that an additional vertical diffusion should be incorporated.

Chapter 6

Wave plus current experiments

6.1 Summary

In this second results chapter, data from the combined wave and current flows are presented. Three currents were studied on their own and were then added to the wave discussed in the previous chapter. All the measurements presented in this chapter were made at ISVA. The PIV negatives were analysed later in Edinburgh. As in the previous chapter a few velocity and vorticity plots are given first. Then the derived velocity profiles and subsequent calculations of an apparent roughness parameter are described. Lastly vortex characteristics are given.

6.2 Velocity and Vorticity Maps

Fig. 6.1 depicts the wave plus strongest current, WC3, at phase $\omega t = 120°$. The wave is travelling from left to right. The currents are all co-directional with the wave. There is a well-formed negative vortex in the lee of the ripple crest, as would be expected when the oscillatory part of the flow has just passed maximum velocity. This is clear again in the corresponding vorticity plot, fig. 6.2.

The time-average of the same flow is given in fig. 6.3. It was obtained by averaging the instantaneous phases over the wave-cycle as described in section 5.3.2. WC3 has a larger mean velocity than for the wave-only case, as would be expected from the addition of a steady flow component, and only one recirculating cell — in the lee side of the steady flow.

One roll of film, 12 pictures, was taken of each of the current-only flows. Fig. 6.4 is the result of averaging the 12 instantaneous measurements for the strongest current, C3. The velocities below crest level are small and increase with height into the flow.

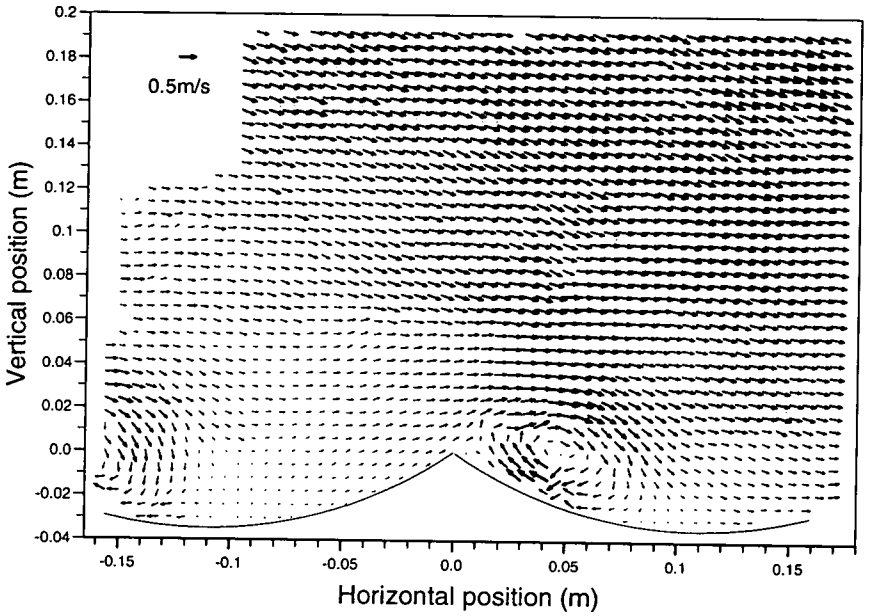

Figure 6.1. Velocity map for wave plus current flow (WC3): orbital wave velocity U_b=280mm/s, current velocity U_c=230mm/s and ωt=120°.

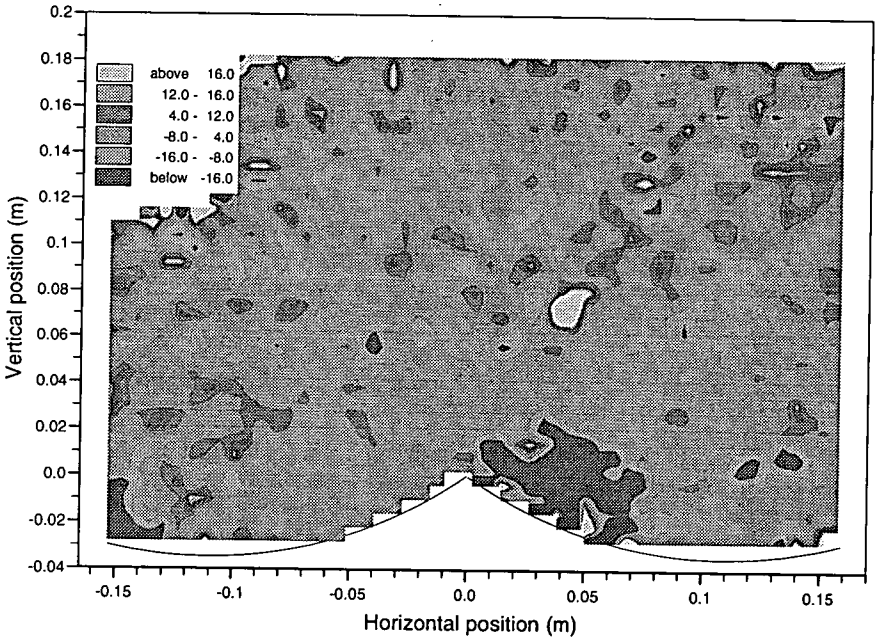

Figure 6.2. Vorticity plot for wave plus current flow (WC3): U_b=280mm/s, U_c=230mm/s and ωt=120°. Vorticity is in s^{-1}.

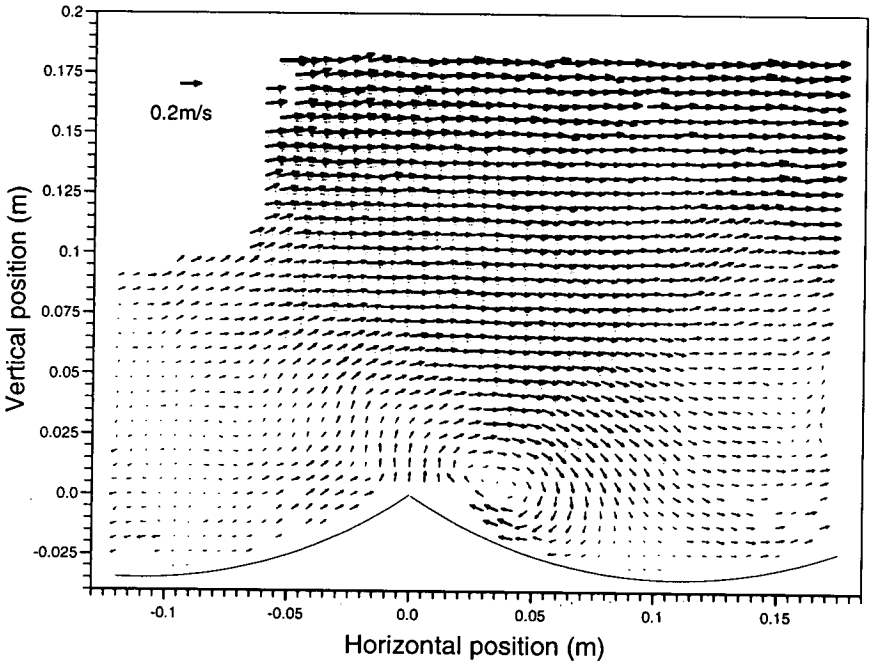

Figure 6.3. Velocity map of time-averaged, wave-current, WC3, flow.

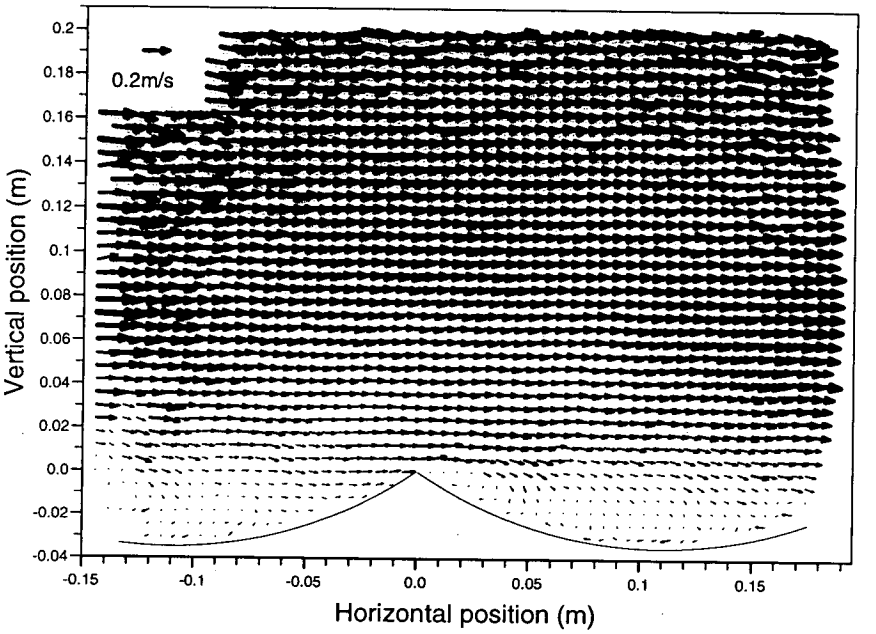

Figure 6.4. Velocity map of averaged flow under C3, the strongest current (U_c=230mm/s).

6.3 Velocity Profiles

Fig. 6.5 shows the comparison of the mean horizontal velocity profiles, calculated as before, of current alone and wave plus current for each of the three currents. Grant and Madsen [19] developed an analytical model to describe combined wave-current flows over a rough bed. The model itself is oversimplified compared with subsequent methods; it assumes certain of the parameters associated with the oscillatory motion are time-invariant. However, they introduce the important concept of an apparent roughness parameter, k_a. The argument for k_a is an extension of the previous one for the physical roughness parameter k_s. The wave on its own has an associated thin, turbulent boundary layer at the bed above which its motion is, to first order, sinusoidal. The current alone, on the other hand, is turbulent throughout the water depth [53]. Hence it can be regarded like a fully developed turbulent flow with an associated boundary layer and therefore a constant shear stress. This layer will extend through most of the flow depth. So, as the oscillatory and steady flows are both turbulent at the bed, they will interact with each other there. The turbulence generated by one will affect the velocity of the other. This interaction is found to be nonlinear [19]; the resultant shear stresses are not the same as those found when either the wave or current occur independently. Thus the separate wave and current flows cannot be simply added together to give the combined flow. The current above the wave boundary layer feels a shear stress which is dependent on the physical bottom roughness and on the wave boundary layer. Grant and Madsen [19] found that a superimposed wave will reduce the effect of a current through the apparent roughness

parameter, k_a. The physical roughness parameter, k_s, was a measure of the increased resistance to the flow due to the presence of the roughness elements and associated varying pressure gradients. The apparent roughness parameter, k_a, is due to the increased resistance because of the nonlinear interaction between the wave and the current at the bed. That is, the current, due to the presence of the wave, will feel a greater resistance above the wave boundary layer than would be expected from k_s. This effect can be clearly seen in fig. 6.5. For each of the three currents, the mean velocity is considerably reduced when the wave is added. The largest reduction in the strongest current, C3, is over 40%.

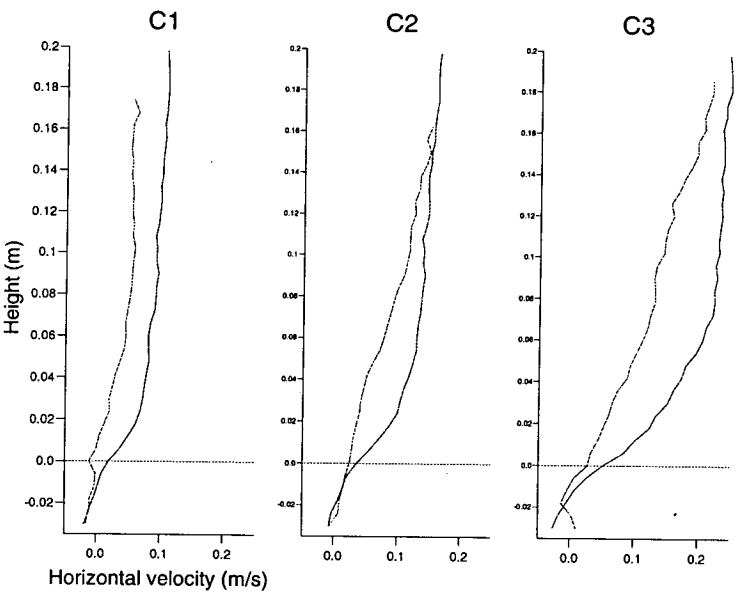

Figure 6.5. Velocity profiles for each of the three currents alone (—) and the same currents with the wave (– –). C3 is the strongest current.

The bed roughnesses, physical or apparent as applicable, and the friction velocities can be determined from the mean velocity profiles for both the current alone and wave plus current cases.

• Current alone

Consider first the current-only cases. The fully developed turbulent flow produced from a steady flow is simply a boundary layer which fills the whole depth [53]. Thus it can be broken down into the three typical boundary layer regions: an inner layer, an overlap layer and an outer layer. The inner, or viscous, sublayer, where viscous stresses dominate, will be very thin, of the order of only a few milimetres. In the overlap layer, the velocity is largely dependent on the shear stress, τ, at the bed. It can be shown [53] that the mean velocity in this layer has a logarithmic profile given, in the case of a rough bed, by

$$\bar{u} = \frac{u_*}{\kappa} \ln \frac{30y}{k_s}. \tag{6.1}$$

The constant $\kappa = 0.4$ is the Von Karman constant and u_* is the friction, or shear, velocity defined in terms of the shear stress, τ by eqn. 5.2. It can be shown [50] that for 2-D flow where $\bar{u} = \bar{u}(y)$, $\bar{v} = \bar{w} = 0$, that the shear stress,

$$\tau = -\rho \overline{u'v'}, \tag{6.2}$$

where u' and v' are the turbulent fluctuations in horizontal and vertical velocity. Thus from eqn. 5.2,

$$u_* = \sqrt{\frac{|\tau|}{\rho}} = \sqrt{|\overline{u'v'}|} \tag{6.3}$$

and so u_*, the friction velocity, gives some measure of the intensity of the turbulent fluctuations.

The shear stress, τ, within a fully developed turbulent boundary layer is constant [41]. Thus from eqn. 5.2 for a particular boundary layer the friction velocity, u_*, is a constant. From eqn. 6.1, semi-log plots of the velocity profiles can be used to determine k_s and u_*. Fig. 6.6 shows the least squares fit to the semi-logarithmic velocity profile data. As in the previous chapter, the reference level for y is 0.3η below the ripple crests. The fit is only for those data points within the overlap layer. The lowest data point is not included in the logarithmic fit to ensure that the inner layer is avoided. At the upper end of the data for the strongest current, C3, beyond the overlap (or log) layer is the outer layer. In general, for a given geometry, the boundary layer will shrink with increasing free stream velocity. From Schlichting [50] the thickness $\delta(x)$ of a turbulent boundary layer over a smooth flat plate at a distance x along the plate is given by

$$\delta(x) = 0.37x \left(\frac{Ux}{\nu}\right)^{-\frac{1}{5}}. \tag{6.4}$$

Jensen et al [29] found that the thickness of the logarithmic layer above a rough bed is smaller than above a smooth bed, so eqn. 6.4 cannot be used here directly. However, the trend will be the same, that is, $\delta(x)$ decreases as U increases at a given distance, x. Physically this is because the boundary layer is the area of the flow, at the plate, where viscous forces dominate over inertial ones. At higher velocities, inertial forces are larger and will therefore outweigh the viscous forces increasingly close to the bed. Thus in fig. 6.6 the top of the overlap layer for

the strongest current, C3, is closer to the bed than for C1 or C2. The boundary layers for the two slower currents appear to be thicker than the measurement depth.

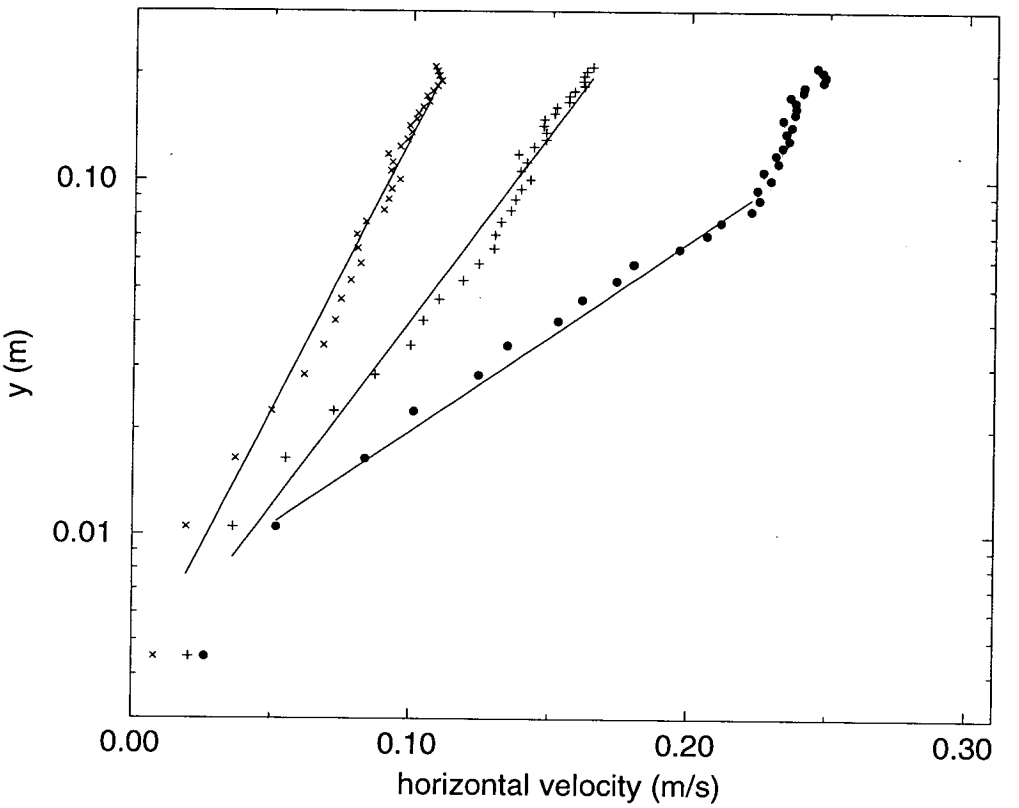

Figure 6.6. Semi-log velocity profiles for current-only with lines fitted to the overlap layers. Symbols: X - C1, + - C2 and • - C3.

• Wave plus current

In the case of combined wave plus current, the time-independent, mean velocity profile can be divided, as described above, into an inner and outer region. The outer region is unaffected by the waves, so has the same form as eqn. 6.1 for the current-only case, that is

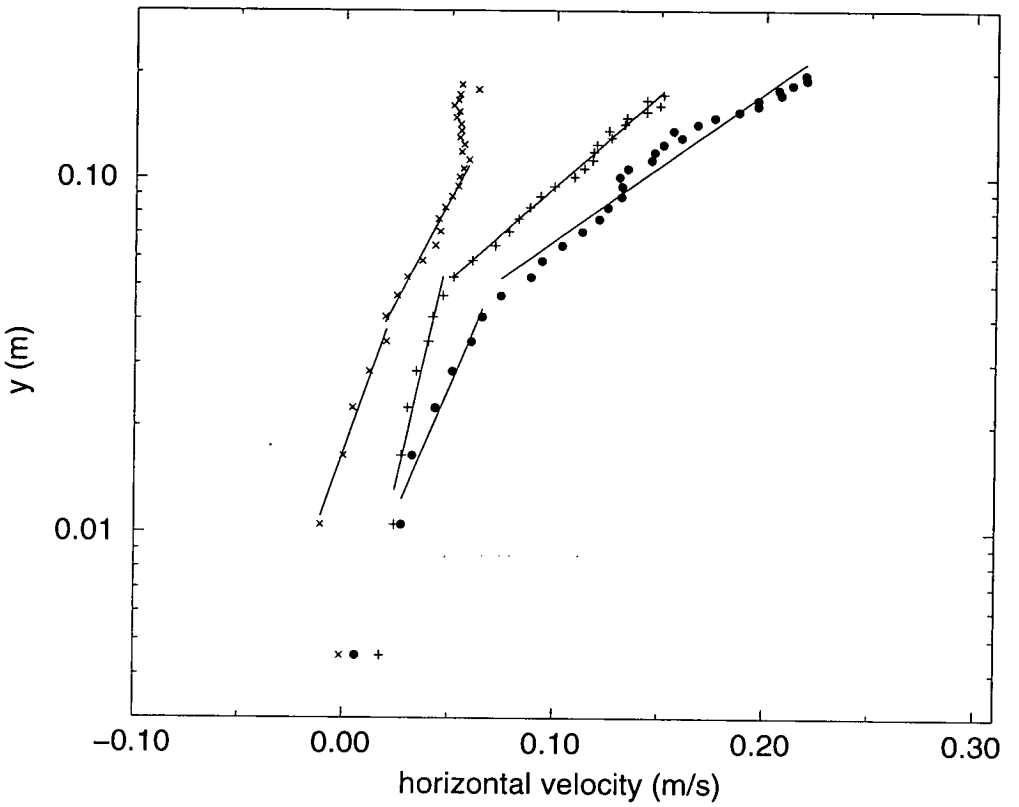

Figure 6.7. Semi-log velocity profiles for wave plus current with lines fitted to the overlap layers. Symbols: X - WC1, + - WC2 and • - WC3.

$$\bar{u} = \frac{u_{*c}}{\kappa} \ln \frac{30y}{k_a}. \tag{6.5}$$

where the physical roughness parameter, k_s, has been replaced by the larger apparent roughness parameter, k_a and u_{*c} is the current friction velocity.

The inner region is dependent on the wave induced boundary layer. There has not been sufficient experimental work to determine the precise form of the velocity profile in this layer. However, various theories have been proposed, several of

	C1	C2	C3
k_s (cm)	12±1	12±1	19±2
u_* (mm/s)	11.5±0.2	16.9±0.3	33.7±0.8
	WC1	WC2	WC3
k_s (cm)	51±8	11±2	19±3
u_{*w} (mm/s)	10±0.4	7.1±0.7	14.0±1.5
k_a (cm)	69±2	84±2	77±2
u_{*c} (mm/s)	15.0±0.2	32.9±0.5	41.6±0.6

Table 6.1. Results for friction velocities and physical and apparent roughnesses.

which find a second log layer to be plausible. In particular, Fredsøe [14, 16] extended his work from the purely oscillatory case discussed in the previous chapter to include a current. He assumed the mean current velocity profile inside the wave boundary layer to be given by

$$\bar{u} = \frac{u_{*w}}{\kappa} \ln \frac{30y}{k_s} \tag{6.6}$$

where u_{*w} is the current friction velocity for the inner profile. Thus by fitting two different log slopes to the mean velocity profiles for the combined wave and current data as in fig. 6.7, k_s, k_a, u_{*w} and u_{*c} can be determined.

The results for all measured friction velocities and roughness parameters are given in table 6.1. The associated errors were determined by fitting alternative, but still plausible, lines to the data points, calculating u_* and k_s for those lines and comparing them to the original results. The friction velocity, u_*, only depends on the gradient of the line and therefore in general is more accurate than

the roughness parameter, k_s, which is a function of the exponential of the intercept. Any slight change to the fitted line changes the intercept and this difference is exacerbated by the exponential function.

For current-only, the friction velocity, found from the gradient of the fitted line, fig. 6.6 increases with increasing mean current velocity from 11.5 ± 0.2 mm/s to 33.7 ± 0.8 mm/s. Values for k_s were found to be 12 ± 1 cm for both C1 and C2 increasing to 19 ± 2 cm for C3, comparable with the value given by the formula used earlier in section 5.3.1: $k_s = 25\eta(\eta/\lambda) = 13.9$ cm. Kemp and Simons [32] carried out a series of experiments with waves and currents over smooth and rough beds using LDA. Their roughness elements were 5 mm high triangular strips glued across their tank at 18 mm intervals (centre to centre) giving a height to length ratio of 0.28, compared to the steepness used here of $\eta/\lambda = 0.16$. They found that in the case of a current alone over their rough bed k_s was 25 mm, five times larger than the roughness element height. This agrees reasonably with the results quoted for this study where five times the ripple height, $5\eta = 17.5$ cm.

Moving on to the combined wave and current flows, it is clear from fig. 6.7 that for WC2 and WC3 there are two distinct slopes. Again the lowest points are ignored to allow for the thin sublayer as explained for the current-only case. It is less clear which lines should be fitted to the WC1 data. It is possible that the two log layers are as shown, which would imply that the upper log layer ends and the non-logarithmic outer layer starts closer to the bed for the slower current. However, the suggested log layers are not obvious from the data for WC1 and would give a surprisingly high value for k_s of 51 ± 8 cm. For WC2 and WC3 the

friction velocity in the outer region, u_{*c}, is higher than that for the current alone, implying a higher shear stress due to the presence of the wave, as expected. The apparent roughness, k_a, is 5–6 times the values found for physical roughness, k_s, under a current alone. Kemp and Simons [32] added waves to their current and found the ratio, k_a/k_s, of apparent roughness parameter to physical roughness parameter to be 1.1–1.6, where k_s is calculated from eqn. 5.3, see table 6.2. Villaret and Perrier [58] measured velocities over sand ripples under combined waves and current using ultrasonic velocimeters. They formed ripples under their required flow conditions, stopped the flow, measured the profiles and then restarted the flow to carry out their experiments. Their ripples were found to be about 6 mm high with $\eta/\lambda = 0.11 - 0.12$. They found values of k_a such that k_a/k_s was in the range 4.5 – 8.9 for their current and range of waves. As k_s calculated in this way (eqn. 5.3) is a function of ripple steepness, Villaret and Perrier's experiments over ripples are a better comparison here than Kemp and Simons' experiments over triangular roughness elements. In the experiments presented here, k_a/k_s was in the range 4.9–6.2.

Grant and Madsen [19] concluded from their model that a wave always influences a co-existing current but that as the current velocity, U_c, increases compared to the wave orbital velocity, U_b, this influence decreases. Lambrakos et al [35] carried out experiments in the Strait of Juan de Fuca, between Washington State and Vancouver Island. They collated data from a wide range of wave/current combinations all of which showed that the wave effect depends on the ratio of U_b/U_c and increases as U_b increases. In the experiments presented, U_b was constant throughout and U_c was varied. As U_c was increased, u_{*c} was found to

	η(cm)	η/λ	k_a(cm)	k_a/k_s
expt	3.5	0.16	69	5.0
			84	6.0
			77	5.5
V & P	0.6	0.12	8.1	4.5
		0.12	12.7	7.1
		0.11	14.2	8.9
K & S	0.5	0.28	0.37	1.1
			0.56	1.6

Table 6.2. Comparison of apparent roughnesses with other experiments. Expt refers to the tests described here, V & P to Villaret and Perrier [58] and K & S to Kemp and Simons [32]. $k_s = 25\eta(\eta/\lambda)$.

also increase. That is, a stronger current induces a larger shear stress as for the current-only cases. It is harder to discern a trend for k_a especially given that the value for WC1, as explained earlier, should be treated with caution. For WC2 and WC3, the values for k_a decrease with increased U_c as the two studies described above predicted. However a trend based on two points is impossible to substantiate.

6.4 Life-cycles of the vortices

It is predicted that in the combined wave and current flows, the negative vortex will dominate throughout. The negative vortex, formed under the forward motion of the wave, will be stronger than the positive one, formed under the trough, as explained in 5.4.1. Following a similar argument to the one discussed in that section, the bulk flow has a positive velocity gradient, as shown in fig. 6.5, and

thus a negative vorticity ($\delta\bar{\omega} = -\frac{\partial \bar{u}_w}{\partial y}$), so the already stronger negative vortex will be further reinforced at the expense of the weaker positive one. In fact, as stated in chapter 2, this bias would produce asymmetric ripples which might then result in slightly larger vortices.

This predicted domination is seen to be true from the velocity and vorticity plots (fig. 6.3 showed only one, negative, recirculating cell) so the vortex characteristic calculations have been carried out for the negative vortices but not the weaker positive ones.

6.4.1 Circulation and radius

The variation of the circulation of the negative vortex with phase for each of the wave plus current flows is given in fig. 6.8. In each case the vortex grows to a maximum strength at or just after 90°, ie just after maximum horizontal velocity. As for the preceding chapter this is in accordance with predictions by Horikawa and Mizutani [25] for sharp crested ripples. The strongest flow has the strongest vortex as would also be expected intuitively. As the flow slows down and the oscillatory part reverses, the vortex decays. They all have a lifetime of about one time period.

It looks from fig. 6.8 as though the vortex from WC1 is initially stronger than that from WC2. Due to problems described earlier in 4.4, some of the data fields have several missing vectors on the bed side of the new vortex whilst it is

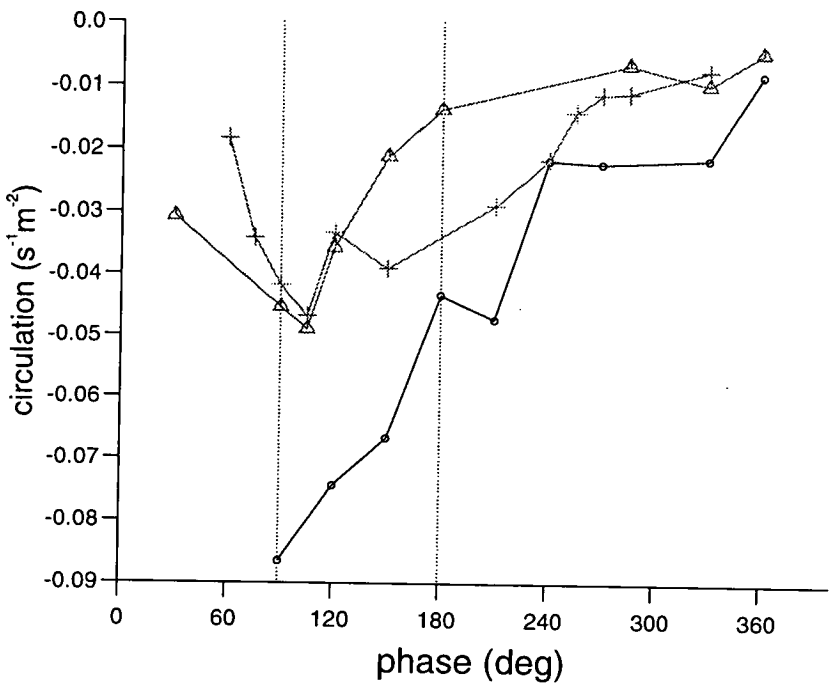

Figure 6.8. Vortex circulation for wave plus current flows against phase of the flow. Symbols as follows: △ - WC1, + - WC2 and • - WC3.

still close to the bed. In particular, the early phases of WC2 each have several missing points which would imply that the WC2 vortex is underpredicted before 120°. There were too many missing points in the early phases of WC3 to make calculations there meaningful.

For similar reasons, the radius data, fig. 6.9, are scattered. As before, this is also the least accurate of the four calculations. There is a trend, however, particularly after the vortices have been shed and the calculations become more reliable, for the three lines to separate out. The strongest current producing the physically largest vortex, the smallest current, the smallest vortex. The radii are

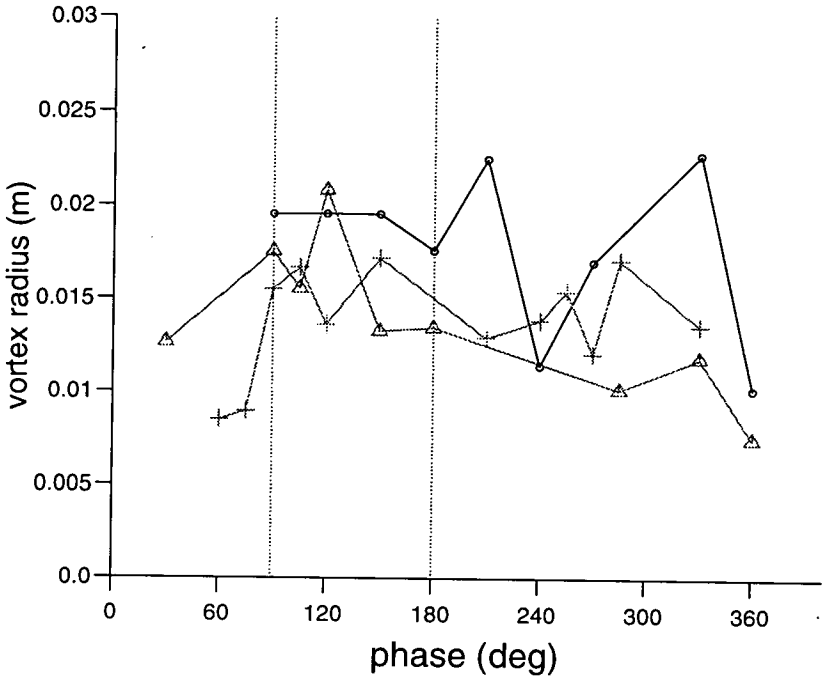

Figure 6.9. Vortex radii for wave plus current flows. Symbols as for fig 6.8: △ - WC1, + - WC2 and • - WC3.

1–2 cm.

6.4.2 Trajectories

The paths of the horizontal and vertical centres of the vortices are given in figs. 6.10 and 6.11. For all these flows, even with the largest current, the vortices move offshore, against the current. The vortex under the weakest current predictably travels furthest, about 17 cm from the 'parent' crest. In the strongest flow, WC3, the vortex only moves a few centimetres. From fig. 6.11, the vortices are lifted slightly higher than for the wave-only case, up to about 7.5 cm in WC3.

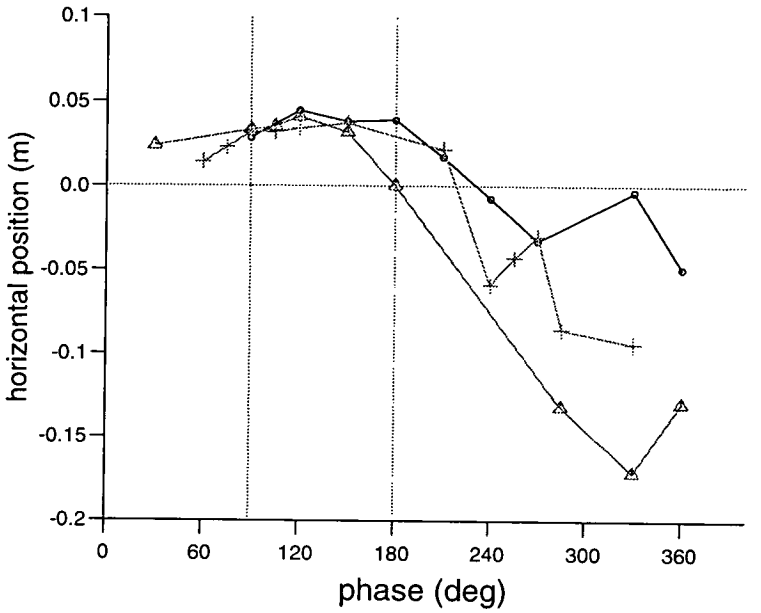

Figure 6.10. X-centre of vortex for wave plus current flows. Symbols as for fig 6.8: △ - WC1, + - WC2 and • - WC3.

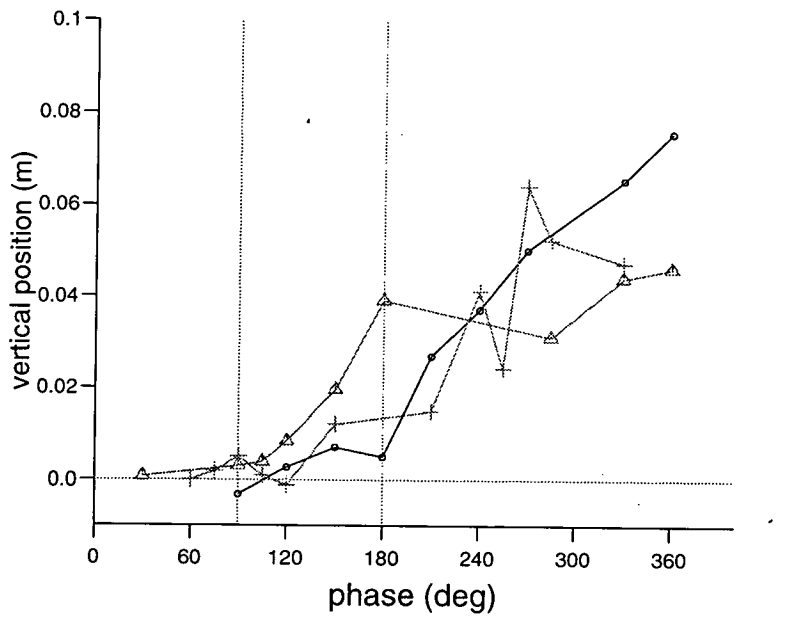

Figure 6.11. Y-centre of vortex for wave plus current flows. Symbols as for fig 6.8: △ - WC1, + - WC2 and • - WC3.

6.5 Concluding Remarks

For this chapter, high quality PIV measurements of combined, collinear wave plus current flows were obtained and used to investigate properties of both the time-independent mean flows and the time-evolution of the vortices.

The current-only flows were shown to have the expected logarithmic layers. The predicted reduction in mean velocity by up to 43% when a wave was superimposed on the currents was also demonstrated. Friction velocities and physical and apparent roughness parameters were determined and found to be comparable to previous researchers' work. Vortex strengths, radii and trajectories were also calculated as for the previous chapter.

Chapter 7

Conclusions

7.1 Summary of main results

Full-field, instantaneous velocity data were obtained at several phases throughout the cycles of several kinds of flow:

- oscillatory
- wave-only
- current-only
- combined wave plus current.

The ripple which was used for all flows fitted the equilibrium conditions for the slower oscillatory flows and for the wave-only flow. For practical reasons the same ripple was also used for the remaining oscillatory cases and for the flows with a steady component. This may lead to slight differences in the shed vortices and

should be taken into account when using the data.

All measurements were made using PIV. The two main aspects of the flows were studied subsequently: the boundary layers and vortices.

• **Boundary layers**

The development of the boundary layers was followed in the oscillatory flows. The boundary layer thickness was measured at each phase and the results were found to compare well with a simple model. The shape of the horizontally- and time-averaged horizontal velocity profile for the wave-only case was shown to have a positive velocity close to the bed which reversed 7 mm above the ripple crests in accordance with Longuet-Higgins' theory [37, 38].

Flows with a steady flow component were shown to have logarithmic layers. By fitting lines to linear-log plots of the cycle-averaged horizontal velocity profiles, the friction velocities and physical and apparent roughness parameters were found. The apparent roughnesses were large, around 20 times the ripple height for the flow conditions considered. Where possible, these calculations were compared to results in the literature and were found to be reasonable.

• **Vortices**

The growing and ejected vortices for all the flows were characterized by their circulation, radius and X- and Y-centres at each phase. These details would have been very difficult, if not impossible, to extract from point measurements acquired with, for example, LDA due to the measurement techniques' inherently

low spatial resolution.

These data for the oscillatory and wave flows were used to assist with validation of a discrete vortex model developed in the University of Wales, Bangor.

7.2 Suggestions for future work

• Measurement technique

PIV has been shown to have many advantages over preceding flow measurement methods, however there is always room for improvement. The next major advance for PIV will be a move from film to video PIV, allowing a much faster frame rate. In the last few years, CCD arrays with a sufficiently high resolution have become available. They are still very expensive but as they become more readily available, video PIV will supersede film PIV. This will have the added advantage of eliminating the need to develop negatives, a procedure which is time consuming and provides an extra opportunity for errors to be made.

The other aspect of the PIV process which could be speeded up is the analysis. Both Fourier transforms could be carried out optically; Jakobsen et al [28] achieve this with the use of an optically addressed spatial light modulator (SLM). Alternatively, Gray [22] acquires multiple images of the flow using a digital camera as described above and then computes the autocorrelations point by point mathematically; analysing 150 points per second compared to the two seconds per point achieved by the analysis system used in this study.

• **Experimental parameters**

The first extension to the work would be to make measurements over a wider range of wave/current combinations to try to determine the trends in the physical and apparent roughness parameters with greater confidence. It would also be interesting to study the effect of rounded crests to check some of the assumptions made throughout about sharp crests.

The wave could also be combined with an opposing current. Kemp and Simons [32], as discussed in the previous chapter, studied the interaction of waves and current when the waves were propagating with the current. They extended their study to the case of waves propagating against a current [33]. They found that the boundary layer is the same in both cases as, close to the bed, the wave motion is oscillatory but that the pattern of vortices, as would be expected, is sensitive to current direction. This could be investigated further.

Bibliography

[1] R.J. Adrian. Scattering particle characteristics and their effect on pulsed laser measurement of fluid flow: Speckle velocimetry vs particle image velocimetry. *Applied Optics*, 23(11):1690–1691, 1984.

[2] R.J. Adrian. Image shifting technique to resolve directional ambiguity in double pulsed velocimetry. *Applied Optics*, 25(21):3855–3858, 1986.

[3] R.A. Bagnold. Motion of waves in shallow water interaction between waves and sand bottoms. *Proc. Royal Society (A)*, 187:1–16, 1946.

[4] M.E. Block. *Wave Generated Flow Over Sand Ripples and the Resulting Entrainment and Suspension of Sediment.* PhD thesis, University of Wales, 1994.

[5] M.E. Block, A.G. Davies, and C. Villaret. Suspension of sand in oscillatory flow above ripples: Discrete-vortex model and laboratory experiments. In *Proc. Euromech 310 Colloquium*, pages 37–52, 1993.

[6] P. Blondeaux. Sand ripples under sea waves. Part 1. Ripple formation. *J. Fluid Mech.*, 218:1–17, 1990.

[7] P. Blondeaux and G. Vittori. Vorticity dynamics in an oscillatory flow over a rippled bed. *J. Fluid Mechanics*, 226:257–289, 1991.

[8] I.H. Broker. Wave generated ripples and resulting sediment transport in waves. Technical Report Series Paper 36, Institute of Hydrodynamics and Hydraulic Engineering, Technical University of Denmark, 1985.

[9] T. Bruce and W.J. Easson. The kinematics of wave induced flows around near-bed pipelines. In *Proc. of 23rd Int. Conf. Coastal Eng.*, pages 2990–2998, 1992.

[10] A.G. Davies and C. Villaret. Oscillatory flow over rippled beds: Boundary layer structure and wave-induced Eularian drift. In J.N. Hunt, editor, *Gravity Waves in Water of Finite Depth*, chapter 6. Computational Mechanics, 1995.

[11] R.G. Dean and R.A. Dalrymple. *Water Wave Mechanics for Engineers and Scientists.* World Scientific, 1991.

[12] C. G. Du Toit and J.F.A Sleath. Velocity measurements close to rippled beds in oscillatory flow. *J. Fluid Mechanics*, 112:71–96, 1981.

[13] H.C. Earnshaw, T. Bruce, C.A. Greated, and W.J. Easson. PIV measurements of oscillatory flow over a rippled bed. In *Proc. 24th Int. Conf. Coastal Eng.*, pages 1975–1982, 1994.

[14] J. Fredsøe. Calculation of mean current velocity profile in combined wave-current motion by application of the momentum equation. Technical Report

Prog. Rep. 55, Institute of Hydrodynamics and Hydraulic Engineering, Technical University of Denmark, 1981.

[15] J. Fredsøe. A simple model for the wave boundary layer. Technical Report Prog. Rep. 54, Institute of Hydrodynamics and Hydraulic Engineering, Technical University of Denmark, 1981.

[16] J. Fredsøe. Turbulent boundary layer in wave-current motion. *J. Hydraulic Eng.*, 110(8):1103–1120, 1984.

[17] J. Fredsøe and R. Deigaard. *Mechanics of Coastal Sediment Transport.* World Scientific, 1992.

[18] C.J. Garrison. A review of drag and inertia forces on circular cylinders. In *Proc. 12th Offshore Technology Conf.*, pages 205–218, 1980.

[19] W.D. Grant and O.S. Madsen. Combined wave and current interaction with a rough bottom. *J. Geophys. Res.*, 84(C4):1797–1808, 1979.

[20] C. Gray. *The Development of Particle Image Velocimetry for Water Wave Studies.* PhD thesis, the University of Edinburgh, 1989.

[21] C. Gray. The evolution of Particle Image Velocimetry. In *Optical Methods and Data Processing in Heat and Fluid FLow*, 1992.

[22] C. Gray. VidPIV for Microsoft Windows - Analysis Tools for Particle Image Velocimetry. Optical Flow Systems Ltd., Technology Transfer Centre, University of Edinburgh, 1995.

[23] C. Gray, C.A Greated, D.R. McCluskey, and W.J. Easson. An analysis of the scanning beam PIV illumination system. *J. Phys. Measurement Science and Technology*, 2:717–724, 1991.

[24] K. Horikawa and S. Ikeda. Characteristics of oscillatory flow over ripple models. In *Proc. 22nd Int. Conf. Coastal Eng.*, pages 661–674, 1990.

[25] K. Horikawa and S. Mizutani. Oscillatory flow behaviour in the vicinity of ripple models. In *Proc. 23rd Int. Conf. Coastal Eng.*, pages 2122–2135, 1992.

[26] P.S. Jackson. On the displacement height in the logarithmic velocity profile. *J. Fluid Mechanics*, 111:15–25, 1981.

[27] M.L. Jakobsen. Private communication, 1996.

[28] M.L. Jakobsen, W.J. Hossack, C.A. Greated, and W.J. Easson. PIV analysis using an optically-addressed spatial light modulator. *Optics and Lasers in Engineering*, 19:253–260, 1993.

[29] B.L. Jensen, B.M. Sumer, and J. Fredsøe. Turbulent oscillatory boundary layers at high reynolds numbers. *J. Fluid Mechanics*, 206:265–297, 1989.

[30] I.G. Jonsson and N.A. Carlsen. Experimental and theoretical investigations in an oscillatory turbulent boundary layer. *J. Hydraulic Res.*, 14(1):45–60, 1976.

[31] R.D. Keane and R.J. Adrian. Optimisation of particle image velocimeters. *Meas. Sci. Technol.*, 1:1202–1215, 1990.

[32] P.H. Kemp and R.R. Simons. The interaction between waves and a turbulent current: Waves propagating with the current. *J. Fluid Mech.*, 116:227–250, 1982.

[33] P.H. Kemp and R.R. Simons. The interaction between waves and a turbulent current: Waves propagating against the current. *J. Fluid Mech.*, 130:73–89, 1983.

[34] H. Lamb. *Hydrodynamics.* Cambridge University Press, 6th Edition 1932.

[35] K.F. Lambrakos, D. Myrhaug, and O.H. Slaattelid. Seabed current boundary layers in wave-plus-current flow conditions. *J. Waterway, Port, Coastal and Ocean Eng.*, 114(2):161–174, 1988.

[36] A.W. Lewis, E. Hitching, G. Perrier, E. Asp Hansen, H. Earnshaw, K. Eidsvik, C. Greated, M. Sumer, and A. Temperville. Flow over vortex ripples: Models and experiments. In *Coastal Dynamics, Gdansk*, pages 686–697, 1995.

[37] M.S. Longuet-Higgins. Mass transport in water waves. *Phil. Trans. Roy. Soc.*, 245(A 903):535–581, 1953.

[38] M.S. Longuet-Higgins. The mechanics of the boundary-layer near the bottom in a progressive wave. In *Proc. 6th Int. Conf. Coastal Eng.*, pages 184–193, 1958.

[39] M.S. Longuet-Higgins. Oscillatory flow over steep sand ripples. *J. Fluid Mechanics*, 107:1–35, 1981.

[40] J.M. Malarkey. Private communication, 1996.

[41] W.D. McComb. *The Physics of Fluid Turbulence.* Oxford University Press, 1990.

[42] I.G. Morrison. *The Hydrodynamic Performance of an Oscillating Water Column Wave Energy Converter.* PhD thesis, University of Edinburgh, 1995.

[43] I.G. Morrison and C.A. Greated. Oscillating water column modelling. In *Proc. of 23rd Int. Conf. Coastal Eng.*, pages 502–511, 1992.

[44] P. Nielsen. Some basic concepts of wave sediment transport. Technical Report Series Paper 20, Institute of Hydrodynamics and Hydraulic Engineering, Technical University of Denmark, 1979.

[45] P. Nielsen. Dynamics and geometry of wave-generated ripples. *J. Geophysical Res.*, 86(C7):6467–6472, 1981.

[46] P.A. Quinn, D.J. Skyner, C. Gray, C.A. Greated, and W.J. Easson. A critical analysis of the Particle Image Velocimetry technique as applied to water waves. In *Proc. of Euromech 279 Colloquium, Delft*, 1991.

[47] K.I.M. Ranasoma and J.F.A. Sleath. Velocity measurements close to rippled beds. In *Proc. 23rd Conf. Coastal Eng.*, pages 2383–2396, 1992.

[48] P.G. Saffman. *Vortex Dynamics.* Cambridge University Press, 1992.

[49] S. Sato, N. Mimura, and W. Watanabe. Oscillatory boundary layer flow over rippled beds. In *Proc. 19th Int. Conf. Coastal Eng.*, pages 2293–2309, 1984.

[50] H. Schlichting. *Boundary Layer Theory.* Pergamon Press, 1955.

[51] D.J. Skyner. *The Mechanics of Extreme Water Waves.* PhD thesis, the University of Edinburgh, 1992.

[52] O.H. Slaattelid, D. Myrhaug, and K.F. Lambrakos. North-sea bottom steady boundary-layer measurements. *J. of Waterway, Port, Coastal and Ocean Engineering*, 116(5):614–631, 1990.

[53] J.F.A. Sleath. *Sea Bed Mechanics.* Wiley, 1984.

[54] I.A. Svendsen and I.G. Jonsson. *Hydrodynamics of Coastal Regions.* Technical University of Denmark, 1980.

[55] D.J. Tritton. Private Communication via F.H.Barnes, 1985.

[56] D.J. Tritton. *Physical Fluid Dynamics.* Oxford University Press, 1988.

[57] E.B. Tunstall and D.L. Inman. Vortex generation by oscillatory flow over rippled surfaces. *J. Geophysical Res.*, 80(24):3475–3484, 1975.

[58] C. Villaret and G. Perrier. Transport of fine sand by combined waves and current: An experimental study. Technical Report Report Number HE-42/92.68, 81pp, Electricité de France, 1992.

[59] G. Vittori and P. Blondeaux. Sand ripples under sea waves. Part 2. Finite amplitude development. *J. Fluid Mech.*, 218:19–39, 1990.

[60] G. Vittori and P. Blondeaux. Sand ripples under sea waves. Part 3. Brick-pattern ripple formation. *J. Fluid Mech.*, 239:23–45, 1992.

Appendix A

Published papers

A.1

H.C. Earnshaw, T. Bruce, C.A. Greated and W.J. Easson. PIV Measurements of Oscillatory Flow Over a Rippled Bed. In *Proc. 24th Int. Conf. Coastal Eng.* pages 1975-1982, 1994.

A.2

H.C. Earnshaw, C.A. Greated and W.J. Easson. PIV Measurements of Flow Over Rippled Beds. In *Proc. MAST-II G8-M Final Workshop, Gdansk. Poland,* Sept. 1995